REVIEW

Check for updates

Mn-based noble metal-free electrocatalysts: advancing the OER and the ORR through innovation and future insights

Anup Bist and Sungjin Park *

Manganese-based electrocatalysts are attracting significant attention as sustainable, earth-abundant candidates for oxygen evolution and reduction reactions in advanced electrochemical energy systems, owing to their low toxicity and versatile redox chemistry. This article provides a comprehensive review of the structural diversity and catalytic potential of Mn-based materials including oxides, chalcogenides, phosphides, nitrides, borides, metal–organic frameworks, and single-atom catalysts while highlighting their environmental compatibility. Key challenges such as low conductivity, limited active site density, structural instability, and suboptimal electronic structure are critically examined. The review places a special emphasis on strategies like defect engineering, heteroatom doping, and electronic modulation particularly tuning the d-band center and e_g orbital occupancy to enhance catalytic performance, achieve balanced adsorption energies, and accelerate reaction kinetics. Notably, several effective solutions, including the integration of conductive supports and hybridization with robust substrates or secondary metals, are demonstrated to improve both efficiency and durability, underscoring the growing promise of Mn-based electrocatalysts for next-generation energy technologies.

1. Introduction

1.1. Fundamentals and the mechanism of oxygen electrocatalysts

The escalating global energy demand, driven by population growth and industrial expansion, has intensified reliance on fossil fuels, accelerating both resource depletion and environmental degradation. To counter these effects, a transition to sustainable energy technologies is essential.[1,2] Electrochemical systems such as water electrolyzers, fuel cells, and metal–air batteries have emerged as promising solutions due to their high efficiency and clean energy output. These systems, however, rely heavily on two sluggish multi-electron processes: the oxygen evolution reaction (OER) and the oxygen reduction reaction (ORR). The OER, which occurs at the anode in alkaline media, involves the oxidation of hydroxide ions (OH^-) to molecular oxygen (O_4). This process follows four key surface-mediated steps: (i) adsorption of OH^- onto the catalyst to form OH^*, (ii) deprotonation to yield O^*, (iii) reaction with another OH^- to form OOH^*, and (iv) decomposition of OOH^* to release O_4 and regenerate the active site.[3–5] These steps are illustrated in Fig. 1(a), which depicts the interaction of oxygen intermediates with catalyst active sites. A more detailed pathway is

outlined in Fig. 1(b), emphasizing the sequential transformations and intermediate states. The high energy barriers associated with these transitions demand significant overpotentials, limiting the overall efficiency.

In contrast, the ORR occurs at the cathode and reduces molecular oxygen *via* either a 4-electron pathway (directly forming OH^-) or a 2-electron pathway (producing H_4O_4 as a byproduct). The process begins with O_4 adsorption (O_4^*), followed by proton–electron coupled steps involving intermediates such as OOH^*, O^*, and OH^*. Catalyst performance in the ORR largely depends on how well these species are stabilized. The competing $4e^-$ and $2e^-$ reaction pathways are illustrated in Fig. 1(a) and the differences in adsorption–desorption behaviour are shown in Fig. 1(c). The $2e^-$ route, often less favourable, can impair selectivity and catalyst stability due to peroxide formation.[6,7] To clarify the thermodynamic demands of both processes, Fig. 1(e) presents a comparative free energy diagram. It visualizes the energy barriers and identifies the rate-determining steps across reaction coordinates. In both cases, achieving an ideal balance in intermediate binding energy is essential; strong binding may block active sites, whereas weak binding can lead to premature desorption, reducing catalytic turnover.[8,9]

Despite notable advancements in electrocatalyst development, key limitations persist such as low conductivity, limited active site availability, and instability under operational

Department of Chemistry and Chemical Engineering, Inha University, 100 Inha-ro, Michuhol-gu, Incheon, 22212, Republic of Korea. E-mail: sungjinpark@inha.ac.kr
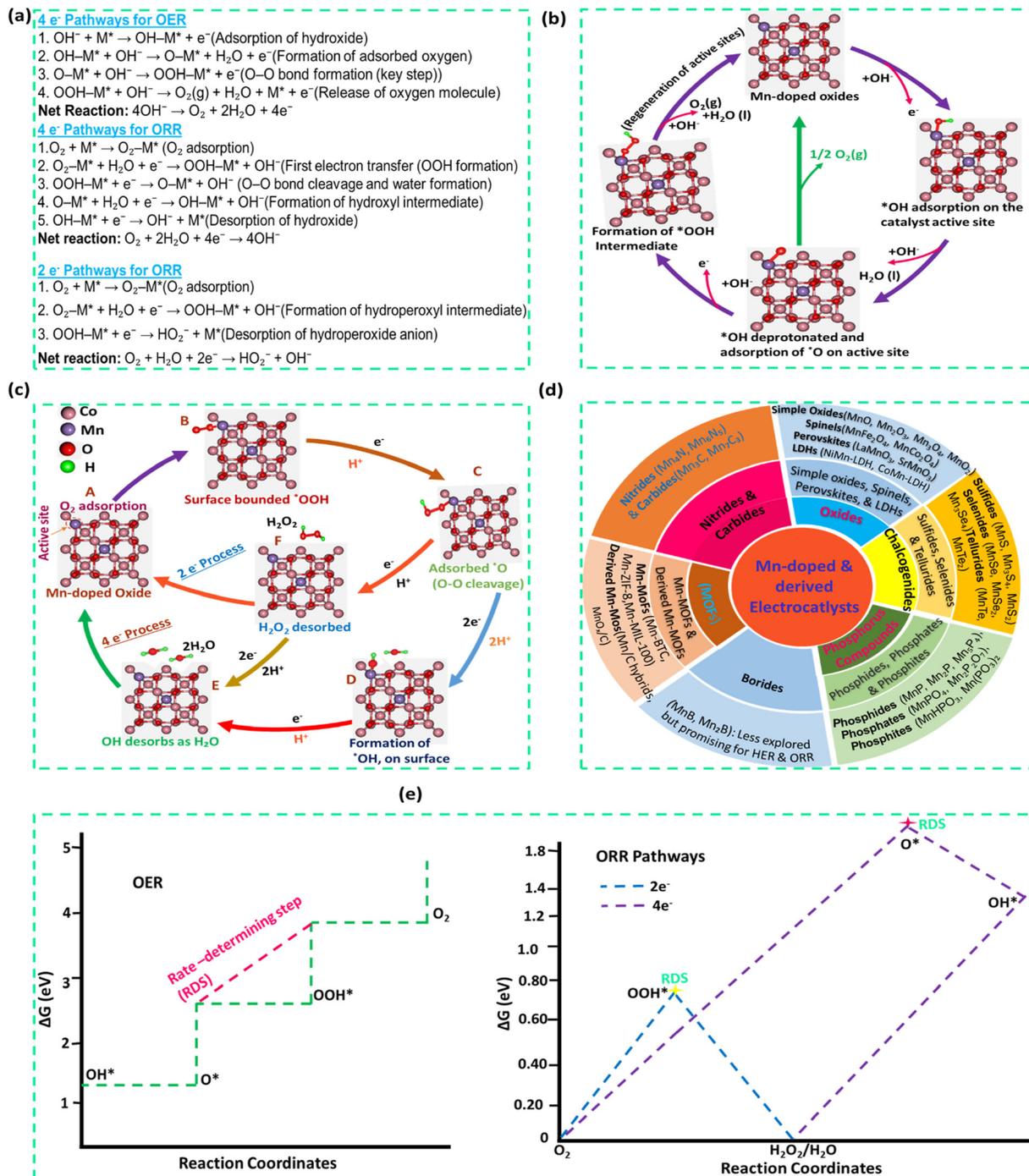
Fig. 1 (a) Scheme illustrating the types of Mn-doped and Mn-derived electrocatalysts. (b) Stepwise reaction mechanisms for the oxygen evolution reaction (OER, 4-electron transfer) and the oxygen reduction reaction (ORR, 4-electron and 2-electron pathways) in alkaline medium. M represents the metal active site involved in intermediate adsorption and electron transfer. (c) and (d) Schematic representation of the reaction mechanisms of Mn-based catalysts for the OER and ORR, respectively. (e) Schematic free energy diagram illustrating the theoretical energy profiles of OER and ORR pathways, highlighting key reaction intermediates and rate-determining steps.

conditions. In the ORR, side reactions and peroxide formation further hinder efficiency and durability. Noble metal catalysts like Pt, IrO_4, and RuO_4 remain the benchmark due to their excellent activity and robustness. However, their cost and scarcity challenge large-scale adoption.[10–12] As alternatives,

earth-abundant transition metals such as Fe, Mn, Co, and Ni offer promising advantages due to their flexible redox states and structural tunability. Among these, manganese-based materials are particularly attractive because of their rich redox chemistry, environmental benignity, and ability to strongly

interact with oxygen species—making them compelling candidates for efficient, durable, and cost-effective bifunctional oxygen electrocatalysts.[13]

1.2. Fundamentals of Mn-based and derived electrocatalysts

Manganese (Mn)-based catalysts have emerged as promising candidates for the OER and ORR owing to their broad range of accessible oxidation states (+2 to +7), enabling dynamic redox transitions and multi-electron transfer processes. This redox flexibility provides Mn-based systems with a competitive edge over conventional transition metal catalysts like Ni, Fe, and Co, which typically operate within narrower oxidation states (+2 to +4), potentially limiting their catalytic performance due to constrained electron exchange capabilities.[14,15] Mn-containing materials exist in structurally diverse architectures, including oxides, metal–organic frameworks (MOFs), single-atom catalysts (SACs), chalcogenides, layered double hydroxides (LDHs), nitrides, and phosphides. These materials can be systematically classified into five categories based on their crystal structure and functional strategy: (i) Mn oxides (*e.g.*, spinels and perovskites), (ii) Mn-based MOFs, (iii) Mn-derived SACs, (iv) Mn-based chalcogenides (sulfides, selenides, and tellurides), and (v) Mn-containing LDHs, nitrides, and phosphides.[16] This classification facilitates a comparative understanding of their intrinsic properties, catalytic efficiencies, and structure–function relationships. For instance, Mn oxides exhibit adaptable redox chemistry; MOFs provide high surface area and tunable coordination; SACs offer atomic precision and maximum atom utilization; chalcogenides enhance conductivity and introduce defect engineering possibilities; while LDHs, nitrides, and phosphides improve ion transport and promote dynamic surface reconstruction. Fig. 1(d) illustrates representative compositions from each class. These materials not only benefit from Mn's redox adaptability but also exhibit favourable adsorption energies for oxygen intermediates (OH*, O*, and OOH*), enhancing catalytic performance, as depicted in Fig. 1(b) and (c). In contrast, Fe- and Co-based analogs often suffer from overly strong binding, leading to sluggish kinetics during intermediate desorption.[17–19] Moreover, Mn-based systems inherently accommodate structural versatility, defect-rich surfaces, and oxygen vacancies, which further boost catalytic activity. For example, $Mn_{0.5}Co_{0.5}Fe_4O_4$ inverse spinel nanocubes feature co-doping-induced oxygen vacancies and a mixed Mn^{2+}/Mn^{3+} redox environment that facilitates O* adsorption, yielding an overpotential of 308 mV at 10 mA cm^{-2} and a Tafel slope of 76.4 mV dec^{-1}, outperforming RuO_4 as an OER benchmark.[20] Similarly, a core–shell Mn/Mn_3O_4 structure introduces lattice strain and interfacial defects, with a significant population of Mn^{3+} (37.5 at%) undergoing disproportionation to Mn^{2+} and Mn^{4+}, generating a highly oxygen-deficient surface beneficial for bifunctional catalysis.[21,22] Doping Mn into frameworks such as oxides, phosphides, or chalcogenides—or conversely, incorporating foreign elements into Mn matrices—can induce lattice distortions and a mixed valency, both of which critically impact catalytic behaviour and stability. For instance, cobalt doping into Mn oxides forms a mixed spinel phase

(Co/Mn $\approx$ 1:1.4) with minimal structural disruption, whereas Mn doping into Co_3O_4 expands the lattice (lattice parameter $\sim$ 8.09 Å), shifts XRD peaks to lower angles, and introduces mixed Co^{2+}/Co^{3+} and Mn^{2+}/Mn^{3+} valencies, enhancing electronic conductivity and charge transfer, as confirmed by XPS and Raman spectroscopy.[23,24] Similarly, La and Sr co-doping in MnO_3 ($La_{0.7}Sr_{0.3}MnO_3$) enlarges the lattice, lowers the d-band centre, and narrows the energy gap to the Fermi level, facilitating better intermediate binding and electron transport.[25] Mn-doped RuO_4 exhibits increased interplanar spacing (from 0.318 nm to 0.327 nm in the (110) plane), crystal distortion, and altered Ru–Mn charge interactions, thereby enhancing OER performance through modulated charge density at Ru sites.[26]

Among Mn-based materials, perovskites (ABO_3-type) stand out due to their flexible crystal structures and defect tolerance, which enable extensive A- and B-site tuning. These features affect porosity, intermediate binding, and catalytic selectivity, while also ensuring long-term durability under alkaline conditions.[27,28] Crucially, two key electronic descriptors—the e_g orbital occupancy and the d-band centre—govern OER/ORR performance by controlling the binding strength of reaction intermediates. An optimal e_g occupancy of $\sim$1.2 provides balanced adsorption: lower values ($<$1.0) result in overly strong binding and hinder desorption, whereas higher values ($>$1.4) weaken adsorption and reduce catalytic activity.[28,29] In parallel, the d-band centre, representing the average energy of occupied d-states relative to the Fermi level, also tunes intermediate adsorption: values too close to the Fermi level cause strong binding and slow kinetics, while too far leads to weak adsorption.[30–32] These parameters vary across Mn-based systems due to differing Mn–X (X = O, S, Se, N, P, and C) bonding environments—for example, Mn chalcogenides (S, Se, and Te) have high d-band centres with strong adsorption; nitrides show moderate-to-high d-band centres; carbides possess low centres favouring weak adsorption; and phosphides provide intermediate binding.[33–35] Notably, Mn incorporation into MOFs such as rGO/FeCo-MOF structures modulates d-band centres, enhances graphitization, and enlarges surface area, thus optimizing catalytic performance.[36] Whether Mn acts as a dopant or host, its presence fundamentally regulates crystal field splitting, oxygen vacancy formation, electronic conductivity, and intermediate adsorption strength. These interrelated features collectively contribute to minimizing the OER–ORR potential gap, advancing the development of cost-effective, durable, and high-performing bifunctional electrocatalysts aimed at sustainable energy technologies.[10–12]

1.3. Synthesis routes and mechanistic insight for Mn-based materials

The synthesis of Mn-based materials encompasses several well-established methods, each offering unique benefits in terms of morphology, scalability, and compositional control. The solid-state reaction method, involving high-temperature calcination of mixed precursor powders, is prized for its simplicity and suitability for large-scale production of robust, well-crystallized

This journal is © the Owner Societies 2025

Phys. Chem. Chem. Phys., 2025, **27**, 17099–17115 | **17101**

materials. This approach also enables the formation of complex multi-principal component alloys (MPCAs) by maximizing entropic effects.[37] The sol–gel method, in contrast, starts with metal alkoxides or salts and proceeds through hydrolysis and gelation, followed by moderate-temperature calcination, allowing precise control over particle size, stoichiometry, and microstructure—ideal for nanostructured oxides and tailored functional properties. Hydrothermal synthesis, performed in sealed autoclaves at elevated temperatures and pressures, stands out for its versatility in producing diverse morphologies and crystalline phases, including hollow and core–shell nanostructures, with excellent phase selectivity and scalability. In addition, vapor-phase techniques such as chemical vapor deposition (CVD) and atomic layer deposition (ALD) are also used to fabricate high-purity Mn-based thin films with atomic-level control, benefiting device applications.[38]

The co-precipitation methods, often conducted in continuously stirred reactors, are favoured for producing Mn-rich precursors with uniform particle size and composition, especially for battery and electrocatalyst applications. This approach is cost-effective, scalable, and enables fine control over elemental distribution, though it requires careful handling to prevent oxidation of Mn^{2+} and impurity formation. Template-assisted synthesis, using hard or soft templates,

provides additional control over nanostructure and porosity, while green or eco-friendly synthesis routes employ benign reagents and mild conditions to minimize environmental impact. Each synthesis strategy offers distinct advantages: solid-state and co-precipitation methods excel in scalability and compositional uniformity; sol–gel and hydrothermal approaches provide superior nanostructure and phase control; and vapor-phase and template-assisted methods enable advanced architectures and device integration. The optimal choice depends on the desired material properties, application requirements, and sustainability considerations.[39,40] A flow diagram summarizes key synthesis routes for Mn-based materials, highlighting their main processes and unique advantages in Fig. 2(a).

Mn-based catalysts exhibit significant mechanistic advantages over classical oxide catalysts for oxygen electrocatalysis, as highlighted in Fig. 2(b)–(d). Unlike traditional oxides that primarily operate through surface adsorbate mechanisms and have limited tunability, Mn-based oxides enable lattice oxygen participation (LOM), possess abundant oxygen vacancies, and allow for e_g orbital tuning via doping or defect engineering (Fig. 2(b)).[41] These attributes lower and make more tunable the rate-determining step energy barrier, leading to enhanced catalytic efficiency, flexibility, and adaptability for
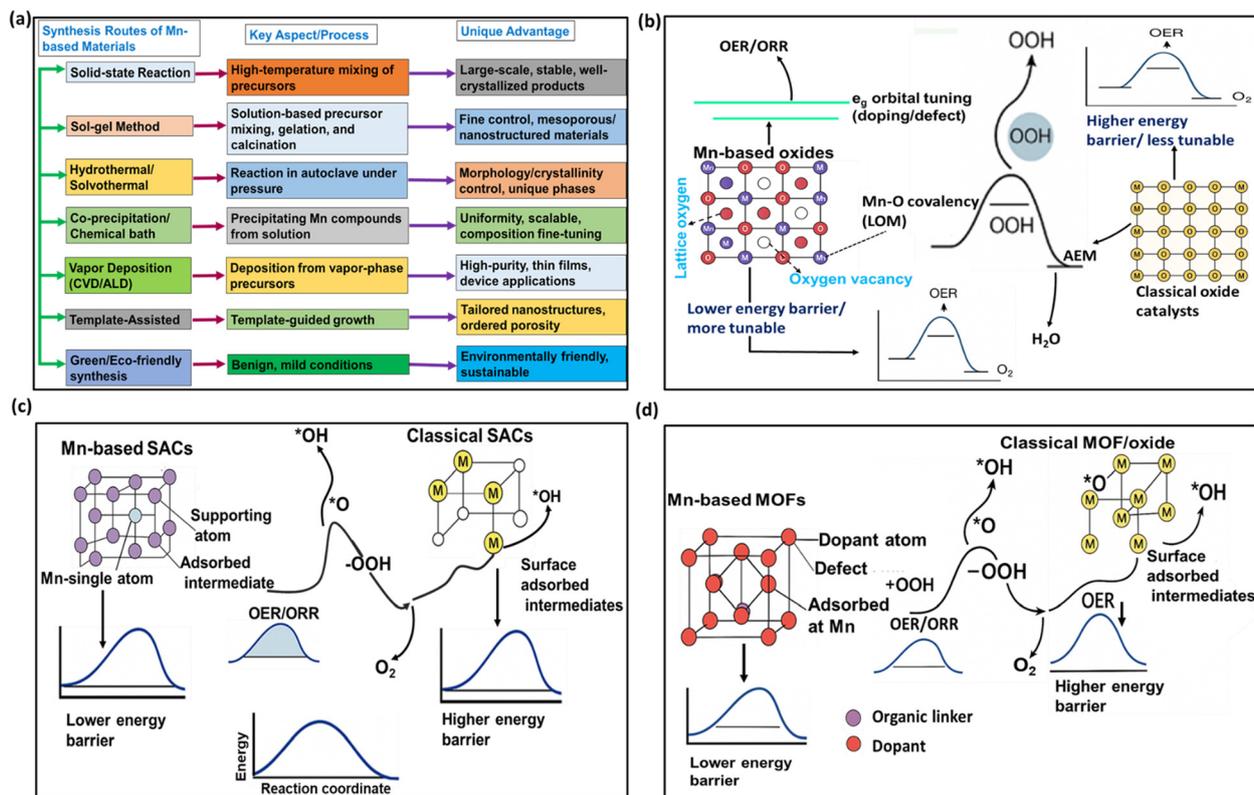

Fig. 2 (a) Flow diagram illustrating the main synthesis routes for Mn–based materials, with key process steps and unique advantages of each method highlighted for comparative insight, (b) Mn–based oxides lower the rate-determining step barrier via lattice oxygen participation, oxygen vacancies, and eg orbital tuning, (c) Mn–based SACs achieve efficient intermediate conversion and reduced energy barriers through atomically dispersed, tailored Mn sites, and (d) Mn–based MOFs provide abundant active sites and tunable environments, enabling lower and more flexible energy barriers than classical catalysts.

17102 | *Phys. Chem. Chem. Phys.*, 2025, **27**, 17099–17115

This journal is © the Owner Societies 2025

the OER/ORR. Similarly, Mn-based SACs feature atomically dispersed Mn centres stabilized by tailored coordination environments, which facilitate efficient adsorption and transformation of key intermediates (such as OH*, O*, and OOH*) and result in a significantly lower energy barrier for the rate-determining step compared to classical SACs (Fig. 2(c)).[42] Furthermore, Mn-based MOFs offer a highly porous structure with atomically dispersed Mn centres, abundant defects, and tunable dopant incorporation, enabling more efficient intermediate adsorption and transformation at Mn sites. This architecture, along with defect and dopant engineering, further optimizes the local electronic environment and achieves a much lower and more tunable rate-determining step energy barrier for the OER/ORR than classical catalysts, as depicted in Fig. 2(d).[43]

2. Mn oxides (simple oxides, perovskites, and spinel-type structures)

Mn-based oxides constitute a structurally versatile class of electrocatalysts, including simple oxides, spinel-type structures, and perovskites. These materials are introduced here based on their crystal structure and composition—starting with simple Mn oxides and progressing through spinels to complex perovskites. This classification highlights how Mn, as a dopant or a core component, regulates the electronic structure—notably the d-band centre and e_g orbital occupancy—as well as the redox chemistry and defect profile. Their performance is further enhanced through compositing with conductive supports and defect engineering, bridging their electronic limitations and strengthening their interrelationship as promising bifunctional OER/ORR catalysts. Mn plays a multifaceted role in oxide electrocatalysts by enhancing both structural and electronic properties. In spinel or hybrid composites, it enables redox flexibility, promotes oxygen vacancy formation, and fine-tunes the d-band centre for optimal catalytic performance. In the Fe–Co@MnO nanobox heterostructure, for example, electronic coupling between the redox-active but poorly conductive MnO and highly conductive Fe–Co leads to a downward shift in the d-band center, optimizing intermediate adsorption during the OER/ORR. This tailored heterointerface improves bifunctional activity by reducing the potential gap between the OER and the ORR (Fig. 2(a) and (b)) and accelerating kinetics, as evidenced by a lower Tafel slope (Fig. 2(c)).[44,45]

Mn oxides inherently offer redox flexibility and structural diversity. Their electrocatalytic activity can be significantly improved by doping or forming composites.[46–48] Zhang et al. demonstrated that Mn doping in Co_3O_4 induces oxygen vacancies and modifies the electronic structure, reducing the OER overpotential from 288 mV to 265 mV at 10 mA cm^{-2}.[49] Spinel-type oxides such as $CoMn_4O_4$, $Mn–Co_3O_4$, and Mn-doped $CuCo_4O_4$ have shown promise, though their intrinsic conductivity is limited. Incorporation with doped carbon nanotubes

(e.g., N-, S-, Zn-doped CNTs) enables efficient four-electron ORR pathways, improving overall bifunctionality.[46,50]

Kang et al. reported that Zn-doped $CoMn_4O_4$/CNT composites showed optimized Mn and Co valence states, achieving a half-wave potential of 0.81 V and an OER overpotential of 312 mV.[51] In another study, Mn-doped $CuCo_4O_4$ was synthesized by alloying–dealloying partially substituted Cu^{2+} ions, creating Cu vacancies and oxygen defects. These changes increased conductivity and active site density, achieving 1.71 V at 500 mA cm^{-2} and operational durability over 80 hours. DFT calculations confirmed that Mn doping elongated the Cu–O bond and shifted electronic density toward the Fermi level, lowering the d-band centre and reducing the OER barrier.[52] Mn-doped Co_3O_4@CNT composites further demonstrated excellent bifunctional performance with an OER overpotential of 356 mV at 10 mA cm^{-2} and an ORR half-wave potential of 0.84 V.[53]

Perovskite oxides offer broad functionality (electronic, magnetic, and ionic) and environmental compatibility, making them attractive for sustainable energy conversion.[54] However, pristine perovskites often suffer from low conductivity and limited active sites. These limitations can be mitigated by transition metal doping (e.g., Zn, Co, Ni, Cu, and Mn). Mn is particularly effective, improving conductivity, creating oxygen vacancies, and increasing redox activity. For instance, Mn doping in $FeTiO_3$ reduced the OER overpotential from 285 mV to 190 mV at 10 mA cm^{-2} and lowered the Tafel slope from 54 to 32 mV dec^{-1}.[55] Gao et al. showed that Mn doping and oxygen vacancies in $LaMnCoO_3$ enhanced crystallinity and electronic structures.[29,56] In their study, substitution of smaller Co^{3+} (0.54 Å) by larger Mn^{3+} (0.66 Å) in $LaMn_{0.3}Co_{0.7}O_3$ (LMCO-1) expanded the lattice (confirmed by XRD). Hydrogen treatment (5% H_4/Ar) generated LMCO-2 with oxygen vacancies and a more favourable local electronic environment. The e_g occupancy decreased from 1.17 in LMCO-1 to 1.01 in LMCO-2, close to the optimal value of 1 for bifunctionality. Mn also promoted a Co^{3+} spin-state transition from intermediate (e_g = 1) to high-spin (e_g = 2), enhancing Co–O bonding. Additionally, the Co^{2+} content increased from 42.77% to 45.2% and the oxygen vacancy concentration increased from 14.65% to 20.24%, both contributing to improved charge transfer.[29,56]

Oxygen vacancies (O_v)—missing lattice oxygen atoms—are important for catalytic activity, while lattice oxygen (O_L) represents the ideal crystalline oxygen. A higher O_v/O_L ratio indicates increased defect density and more active sites. As shown in Fig. 2(d), this enhances electrocatalytic performance. In DFT calculations comparing Mn–doped np–$Cu_{10}Co_{40}$(Mn) with its oxygen-deficient version (Ov–np–$Cu_{10}Co_{40}$(Mn)), the OOH → O_4 transition energy dropped from 4.4 to 2.69 eV (Fig. 2(e) and (f)). The d-band centre shifted upward from −3.71 to −3.36 eV, signifying improved electronic interaction and higher activity.[52]

Sun et al. explored Mn–Ni co-doping in $LaMnNiCoO_3$ perovskites, revealing that this tuning modulates e_g electron filling and shifts the O 2p-band closer to the Fermi level—key factors in electrocatalysis.[28] Co-doping also introduced multiple valence states (Mn^{3+}/Mn^{4+}, Co^{2+}/Co^{3+}, and Ni^{2+}/Ni^{3+}), increasing redox flexibility.

This journal is © the Owner Societies 2025

Phys. Chem. Chem. Phys., 2025, **27**, 17099–17115 | **17103**

The optimal $LaMnNiCoO_3$ (1:2:3) composition achieved an e_g occupancy of 1.086, near the ideal 1, whereas a higher/lower Ni content deviated from this optimum. Additional oxygen vacancies and stronger metal–oxygen covalency improved OER/ORR kinetics.

In another study, Mn substitution in $SrFe_{1-x}Mn_xO_{3-\delta}$ increased reactive oxygen species (O^{2-}/O^-) from 17.4% to 24.5%, improving CO_4 resistance and ORR activity.[58] A $LaMnO_3/Mn_4O_3$–carbon black composite prepared by the sol–gel method also demonstrated excellent ORR activity due to synergistic Mn^{4+}/Mn^{3+} redox effects and improved conductivity. The catalyst had an onset potential of 0.87 V, a Tafel slope of 90 mV dec^{-1}, and followed a favourable four-electron pathway.[59]

Finally, Mn doping in perovskite structures generates oxygen vacancies (Fig. 2(g)) and optimizes both the e_g orbital occupancy and d-band centre. These electronic modifications enhance active site availability, charge transport, and conductivity, enabling superior bifunctional OER/ORR performance with competitive activity (Fig. 2(h)) and robust long-term durability (Fig. 2(i)).

3. Mn-based metal organic frameworks

Following Mn-based oxides and LDHs, MOFs represent a structurally distinct class of materials offering diverse strategies for tuning electrocatalytic activity. This section is organized based on the catalyst origin—pristine MOFs, MOF-derived composites, and multi-metallic MOFs—with a focus on how Mn incorporation affects the electronic structure, particularly through d-band centre alignment, oxidation state flexibility, and synergistic effects with other metals. These characteristics not only unify the different MOF-based platforms but also interlink with broader design strategies discussed throughout this review.

MOF-based electrocatalysts have been extensively explored for the OER and ORR due to their unique structural and electronic features, which include: (i) high porosity and surface area, (ii) tailorable metal centres, (iii) effective synergy and electronic modulation, and (iv) high stability and capacity for defect engineering. The high surface area and porosity facilitate rapid diffusion of O_4 and OH^- from the electrolyte to active sites. Transition metals like Fe, Co, Ni, and Mn embedded in MOFs act as catalytic centres, enabling water adsorption, activation, and proton–electron transfer during the OER and ORR, as shown in Fig. 3(a). Additionally, organic ligands in MOFs help modulate the electronic structure of the metal sites, optimizing adsorption/desorption of intermediates.[60]

Hybrid MOF structures integrated with conductive carbonaceous materials—such as graphene, carbon nanotubes, or other forms of carbon—significantly enhance electron transport during redox reactions. This enhancement is due to improved porosity, mass transport, and electrolyte penetration, all of which contribute to greater active site exposure. A

representative example is the Co–Mn metal atom-incorporated N-doped microporous carbon synthesized via one-step pyrolysis, referred to as CoMn-N-C-Ac-2-800 (Fig. 3(b) and (c)). This material exhibits superior onset and half-wave potentials compared to the benchmark Pt/C catalyst, achieving a half-wave potential of 0.875 V, as shown in Fig. 3(d).[61]

Some pristine MOFs, however, suffer from poor conductivity and lower stability, which can be overcome through derivatization and doping strategies. Mao et al. reported a FeCoNiMn-MOF, a tetra-metallic structure synthesized with 2,3-dihydroxyterephthalic acid as a ligand. The ligand coordinates with metals, enhancing metal coordination geometry, stability, and conductivity. Solvents were used to control morphology and porosity. Mn serves as a secondary metal centre, supporting crystal growth, porosity, and the tuning of the electronic structure. Due to Mn's flexible oxidation states, this MOF exhibited improved charge distribution and synergistic effects, enhancing the density of active sites.[62] The FeCoNiMn-MOF/NF showed an overpotential of 239 mV at 50 mA cm^{-2} (Fig. 3(e)) under alkaline conditions and a Tafel slope of 62.05 mV dec^{-1}, with long-term stability over 100 hours.[62]

Iqbal et al. reported Mn-doped Ni-MOFs with varying Mn concentrations, such as Mn-MOF, Mn_1Ni_4-MOF, and $Mn_{4.5}Ni_{4.5}$-MOF and compared their electrocatalytic performances. All these exhibited bifunctionality for the OER and ORR. For the ORR, Mn-MOF showed onset and half-wave potentials of 0.89 V and 0.83 V, respectively, with a Tafel slope of 96.8 mV dec^{-1}. Mn_1Ni_4-MOF yielded 0.86 V and 0.80 V with a Tafel slope of 90.2 mV dec^{-1}. The best-performing $Mn_{4.5}Ni_{4.5}$-MOF exhibited an onset potential of 0.87 V, a half-wave potential of 0.81 V, and a Tafel slope of 76.9 mV dec^{-1}. For the OER, the overpotentials at 10 mA cm^{-2} were 394 mV, 431 mV, and 339 mV, respectively. The $Mn_{4.5}Ni_{4.5}$-MOF also showed outstanding durability over 7500 s in the chronoamperometry test and 2000 cycles in the CV test, which were attributed to the synergistic effect of Mn doping in Ni-MOF.[64]

A MOF-derived 3D porous dodecahedral structure, analogous to ZIF-67, composed of Mn/Co–C–N with different Mn/Co ratios (1:1, 1:2, and 1:3), was synthesized via high-temperature carbonization at 600 °C. The Mn/Co–C–N (1:2) catalyst maintained ideal morphology, developed MnO on the ZIF surface, and showed strong Mn–Co coordination. Carbonization improved conductivity, porosity, and surface area. This optimized catalyst achieved the best ORR performance, with an onset potential of 0.89 V and a half-wave potential of 0.80 V, a Tafel slope of 60 mV dec^{-1}, and excellent durability— retaining performance after 10 000 cycles with only an 8-mV shift in $E_{1/4}$.[65]

In another study, a Mn-loaded FeCo-MOF composite with reduced graphene oxide (rGO) was synthesized. The 3 wt% rGO–MnFeCo-MOF demonstrated improved OER activity, with an overpotential of 178 mV at 10 mA cm^{-2}, compared to 270 mV for 3 wt% rGO–FeCo-MOF. For the ORR, 3 wt% rGO–MnFeCo-MOF showed a half-wave potential of 0.74 V, while its Mn-free counterpart showed 0.83 V. Despite a slightly lower $E_{1/4}$, the Mn-doped sample outperformed overall, due to higher limiting
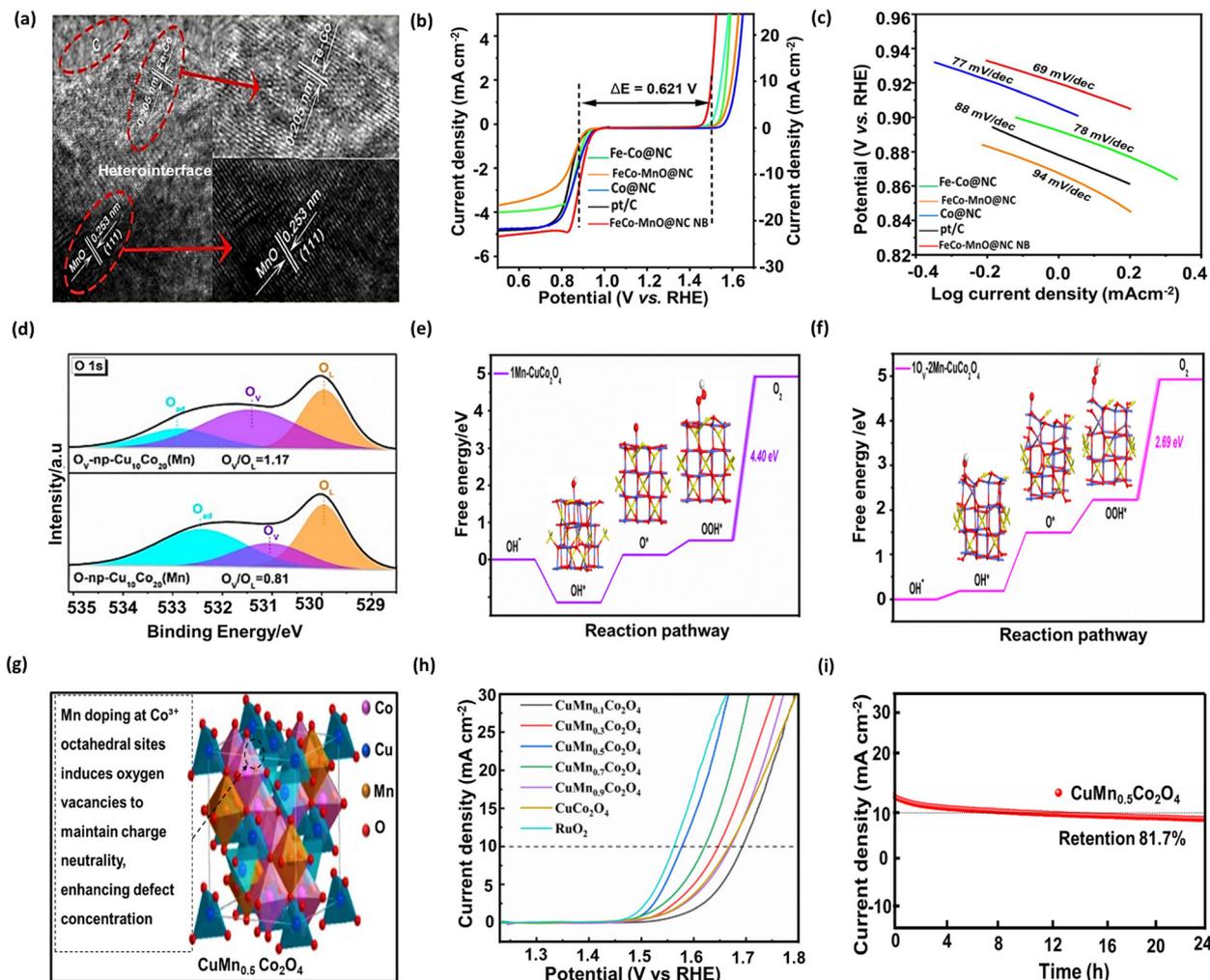
17104 | Phys. Chem. Chem. Phys., 2025, 27, 17099–17115

This journal is © the Owner Societies 2025

Fig. 3 (a) HRTEM image of the FeCo−MnO@NC nanobox heterostructure. Reproduced from ref. 57 with permission from Elsevier, Copyright 2023, (b) OER and ORR polarization curves showing the onset potential difference. Reproduced from ref. 57 with permission from Elsevier, Copyright 2023, (c) Tafel slopes of FeCo−MnO@NC nanobox and reference catalysts. Reproduced from ref. 57 with permission from Elsevier, Copyright 2023. (d) XPS analysis showing increased O_V/O_L ratio with oxygen vacancies enhancing intermediate adsorption. Reproduced from ref. 52 with permission from American Chemical Society, copyright© 2023, (e) and (f) Gibbs free energy profiles indicating reduced O_4 formation energy on vacancy-rich structures. Reproduced from ref. 52 with permission from American Chemical Society, copyright© 2023, (g) Mn-doped spinel structure promoting oxygen vacancy formation and structural optimization. (h) and (i) LSV curves and 24 h stability test of $CuMn_{0.5}Co_4O_4$. Reproduced from ref. 46 with permission from the authors ChemElectroChem Published by Wiley-VCH-GmbH, copyright 2022.

current density (8.74 mA cm^{-2}), lower charge-transfer resistance (34.27 Å), and a smaller potential gap (0.66 V). This was attributed to enhanced active site density, better charge redistribution from Mn doping, and increased conductivity from rGO.[36] Boride-based electrocatalysts integrated with MOFs have also shown promise. A nitrogen-doped porous carbon (NC) derived from Co-MOF exhibited moderate OER performance. In contrast, Co_xMn_yB, derived from similar MOFs showed enhanced kinetics with a Tafel slope of 62 mV dec^{-1} and excellent stability over 12 hours. The improvement was linked to the NC framework, which increased conductivity, and the metal–metalloid bonding in the boride, which helped modulate the electronic structure.[66]

Importantly, Mn in MOFs helps optimize the d-band centre, which governs the interaction between active sites and reaction intermediates. By tailoring Mn's oxidation states and the coordinating environment, both charge redistribution and orbital occupancy (*e.g.*, e_g filling) can be finely tuned. These modifications enhance the adsorption/desorption balance of OER/ORR intermediates, improving reaction kinetics, lowering overpotentials, and ensuring durable operation.

4. Mn derived single atom-based catalysts

This section focuses on Mn-based SACs, classified under functional strategy-driven electrocatalysts that exploit atomic-level precision to enhance the OER and ORR performance. SACs, particularly those derived from Mn or doped with Mn, are
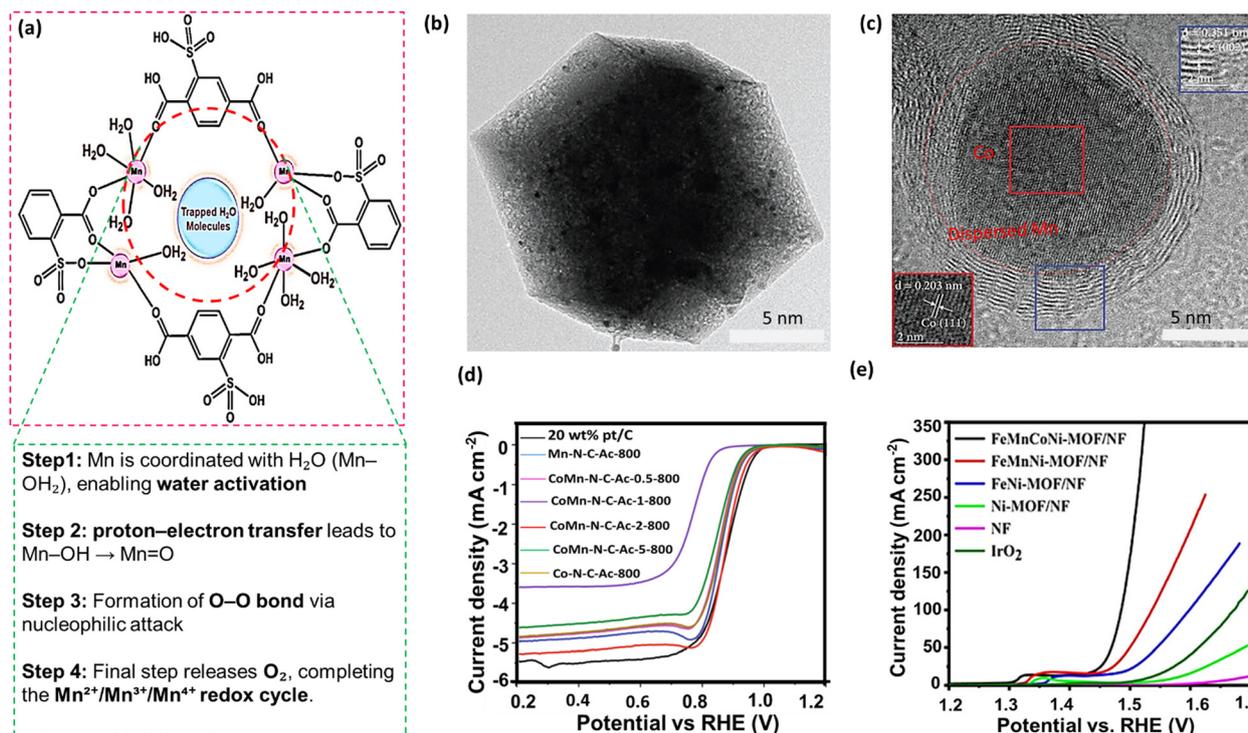
This journal is © the Owner Societies 2025

Phys. Chem. Chem. Phys., 2025, **27**, 17099–17115 | **17105**

Fig. 4 (a) Schematic illustration of the adsorption–desorption mechanism of oxygen intermediates on the Mn-based MOF. Reproduced from ref. 63 with permission from American Chemical Society, Copyright© 2024, (b) SEM image of the CoMn-N-C-Ac-2-800 MOF displaying a rhombic dodecahedron-like morphology. Reproduced from ref. 61 with permission from Wenzhe Luo *et al.*, copyright© 2023. (c) HRTEM images reveal well-defined lattice fringes corresponding to Co and C, with Mn atoms uniformly dispersed throughout the structure. Reproduced from ref. 61 with permission from Wenzhe Luo *et al.*, copyright© 2023, (d) LSV plot showing the superior half-wave potential of CoMn-N-C-Ac-2-800 compared to 20 wt% Pt/C and related materials for the ORR. Reproduced from ref. 61 with permission from Wenzhe Luo *et al.*, copyright© 2023, and (e) LSV polarization curves of FeMnCoNi–MOF/NF compared with IrO_4 and other counterparts. Reproduced from ref. 62 with permission from American Chemical Society, copyright© 2024.

distinguished by their high atomic utilization, electronic tunability, and maximized exposure of active sites. Compared to other Mn-based systems such as oxides and MOFs, SACs offer a platform to understand structure–activity relationships at the atomic scale, especially in heteroatom-coordinated environments (*e.g.*, Mn–N$_4$, Mn–O$_4$).[67,68] These catalysts bridge the gap between molecular and bulk catalysts, enabling efficient modulation of electronic structure for bifunctional activity.

SACs are widely utilized for the OER and ORR due to their well-defined coordination environment and metal–support interactions. In particular, Mn shows excellent synergy with noble metals, forming dual-site SACs that lower energy barriers by facilitating optimal adsorption/desorption of OER intermediates (OH*, O*, and OOH*) as shown in Fig. 4(b).[69] For instance, the Ru–Mn dual-site SAC Ru$_{(SA)}$-NiOMS, integrated into a tunnel-structured Ni ion framework, enables direct intramolecular oxygen coupling, a deviation from conventional adsorbate evolution mechanisms (AEM). This catalyst exhibits a record-low overpotential (160 mV at 10 mA cm^{-2}), a Tafel slope of 32.78 mV dec^{-1}, and a superior mass activity (18 966 A g^{-1}), with prolonged stability over 300 h (Fig. 4(c)).[69]

For the ORR, Mn-doped Fe–N–C catalysts (Mn$_1$@Fe–N–C/CNTs) have been shown to enhance durability by scavenging radicals (•HO$_4^-$, •OH) and stabilizing Fe–N$_x$ sites.[70,71] The

Mn–N$_4$O$_4$ moieties modulate the Fe electronic environment, exhibiting a high $E_{1/4}$ of 0.89 V *vs.* RHE and a narrow ORR–OER potential gap of 0.59 V at 10 mA cm^{-2}.[72] Similarly, Wei *et al.* demonstrated the dual-functionality of Mn single atoms in Pt$_{NP}$–Mn$_{SA}$/C SACs, improving O–O bond cleavage and reducing Pt–O interaction strength, leading to excellent ORR activity ($E_{1/4}$ = 0.93 V, onset = 1.01 V), outperforming Pt/C (Fig. 4(a)).[73]

A variety of Mn-based SAC architectures have been explored. The Pt@Mn$_{SA}$/N–C system exhibited ORR mass activities 11.1 and 14.7 times higher than Pt/C in acidic and alkaline media, respectively.[74] Mn$_{SA}$/Mn$_{AC}$-SSCNR a 3D "sea urchin-like" structure combining Mn single atoms and atomic clusters—demonstrated $E_{1/4}$ = 0.90 V and onset = 0.97 V with excellent retention (91% over 50 h, Fig. 4(d)).[75] The Mn–N@Gra-L catalyst, incorporating Mn–N$_4$ moieties into a mesoporous carbon shell, further enhanced activity and stability ($E_{1/4}$ = 0.875 V, 98.2% retention after 10 000 s).[76] In another study, CoMn/NC SACs with dual atomic sites outperformed Co/NC and Mn/NC individually ($E_{1/4}$ = 0.89 V in KOH, 0.82 V in H$_4$SO$_4$) due to synergy between Co and Mn, supported by DFT calculations showing lower overpotential and favourable oxygen adsorption.[60,77] In FeNPs/MnFe-SAS-NC-25, Mn/Fe dual SACs and Fe nanoparticles cooperatively improved ORR activity ($E_{1/4}$ = 0.91 V) and stability *versus* Pt/C.[78]

17106 | *Phys. Chem. Chem. Phys.*, 2025, **27**, 17099–17115

This journal is © the Owner Societies 2025

Pyrrole-type Mn–N$_4$ (PT-MnN$_4$) catalysts also offer excellent ORR performance across media ($E_{1/4}$ = 0.88 V in alkaline; 0.73 V acidic; 0.63 V neutral) with low Tafel slopes and high durability.[79] Active site confirmation using SCN$^-$ poisoning and DFT analysis confirmed a favourable four-electron mechanism with a low energy barrier (ΔG = −0.39 eV). Under potential cycling, Mn-SASs dynamically evolve from Mn–N$_4$ to Mn–N$_4$C$_4$ configurations, aligning with Mn valence changes and promoting activity (TOF = 1.59 s^{-1} at 0.85 V).[80,81] FeMn$_{ac}$/Mn–N$_4$C, featuring FeMn clusters anchored on Mn–N$_4$ moieties, displayed strong O–O bond cleavage and high $E_{1/4}$ in both KOH (0.90 V) and H$_4$SO$_4$ (0.79 V), alongside superior durability (Fig. 4(e)).[82]

However, Mn-based SACs offer tunable coordination environments and dynamic structural adaptability. Their remarkable performance arises from their ability to modulate the d-band centre and e$_g$ orbital occupancy through strategies like heteroatom doping, dual-atom engineering, and oxidation-state tuning. These approaches enable improved intermediate adsorption and rapid charge transfer, making Mn-SACs highly efficient and durable electrocatalysts for the OER and ORR.

5. Mn-based chalcogenides (sulphites, tellurides, and selenides)

Among the various categories of Mn-based electrocatalysts, chalcogenides—including sulfides, selenides, and tellurides—stand out for their flexible electronic structures and unique redox chemistry. This section focuses on these materials as distinct materials classified by anion composition (S, Se, Te) and their strong Mn–chalcogen bonding, which facilitates redox modulation, defect engineering, and electronic structure regulation. Following oxides, MOFs, SACs, and LDHs, Mn-based chalcogenides represent a material family where d-band centre tuning, vacancy engineering, and heteroatom doping converge to enhance bifunctional activity toward both the OER and ORR.

Mn-based chalcogenides are emerging as highly promising electrocatalysts due to their tunable electronic configurations, robust Mn–S, Mn–Se, and Mn–Te bonds, and their ability to modulate oxidation states, enhancing conductivity and reactivity. These materials benefit from valence flexibility and phase engineering (crystalline vs. amorphous), which enables control over active site exposure and band structure, making them competitive with noble-metal systems. Studies using X-ray photoelectron spectroscopy (XPS) and optical analysis confirm Mn^{2+} incorporation into CdS-type chalcogenides, introducing oxygen vacancies, narrowing band gaps, and tuning the d-band centre to improve charge transfer and catalytic kinetics.[83,84]

A critical aspect of their performance lies in anion vacancy engineering, which generates unsaturated metal sites and optimizes intermediate adsorption energies.[85–88] For example, MnX$_4$/C-HPNs (MnS$_4$, MnSe$_4$, MnTe$_4$) possess 3D hierarchical architectures with abundant vacancies and exposed active sites. These features, alongside Mn^{2+}/Mn^{3+} redox transitions, improve conductivity and OER performance. Notably, MnTe$_4$/C-HPNs achieves an overpotential of 246 mV at 10 mA cm^{-2} and a Tafel slope of 48 mV dec^{-1}, which further improves with 3.1% Fe doping, reducing the overpotential to 210 mV.[89]

Electron redistribution via heteroatom doping also modulates the electronic structure. For instance, MnS/CoN$_x$ exhibits an increased Mn^{4+} content, enhanced electron density, and a shift in the Co 2p binding energy, improving conductivity and d-band positioning.[90] Similarly, MnS–MnO@NSC nanocubes integrate Mn-based compounds into N,S-doped carbon, thereby increasing defect density, electrical conductivity, and catalytic performance.[91] Phase boundary engineering is another effective strategy, Mn doping in Ni$_3$S$_4$@MoS$_4$ nanorods induces interfacial defects between crystalline and amorphous regions, evidenced by Raman red-shifting, which improves conductivity and aligns the d-band centre for optimal OER kinetics.[92] Sm-doped MnTe further illustrates the power of electronic structure regulation: Sm incorporation tunes the d-band centre, introduces lattice oxygen vacancies, and promotes charge redistribution. As a result, this catalyst exhibits an overpotential of 177 mV at 10 mA cm^{-2} and a low Tafel slope of 34 mV dec^{-1}, with stable performance over 40 hours.[93] Rasool et al. reported a Mn-based chalcogenide composite delivering an even lower OER overpotential of 170 mV and a Tafel slope of 32 mV dec^{-1}. Its stability over 5000 cycles (60 hours) underscores the robustness of electronic tuning via Mn incorporation.[94] The excellent long-term durability of Mn-doped chalcogenides is confirmed by linear sweep voltammetry (LSV) and chronoamperometry data (Fig. 5(a) and (b)).

Although the ORR performance of Mn-based chalcogenides is less explored, recent studies indicate strong potential, particularly due to their ability to favor four-electron pathways, provide high onset and half-wave potentials, and maintain excellent durability. The MnSe@MWCNT catalyst demonstrates this promise in O$_4$-saturated 0.1 M KOH, showing an onset potential of 0.94 V and a half-wave potential of 0.86 V vs. RHE, alongside a limiting current density of 6.49 mA cm^{-2}. Koutecky–Levich and rotating ring-disk electrode (RRDE) analyses confirm a four-electron mechanism with minimal H$_4$O$_4$ yield (<10%). The integration of MWCNTs enhances electron transport, provides additional active sites, and yields a low Tafel slope of 54.76 mV dec^{-1}. It retains 95.04% of its $E_{1/2}$ after 12 hours, outperforming Pt/GCE, which shows a 20 mV drop.[95]

Similarly, MOF-derived CoTe$_4$/MnTe$_4$ nanorods show remarkable ORR activity in 0.1 M KOH, with an onset potential of 0.96 V and a half-wave potential of 0.81 V vs. RHE—slightly lower than those of Pt/C but significantly better than those of CoTe$_4$ or MnTe$_4$ alone. The catalyst exhibits a Tafel slope of 64.2 mV dec^{-1}, a high limiting current density of 4.1 mA cm^{-2}, and a nearly ideal four-electron pathway ($n \approx 3.8$), maintaining $E_{1/2}$ with negligible decay after 25 000 s of chronoamperometry.[86]

Taken together, these studies highlight that Mn-based chalcogenides, especially those integrated with conductive supports or doped with heteroatoms, enable precise tuning of the d-band centre and electronic structure, resulting in significant improvements in OER/ORR kinetics. This includes low
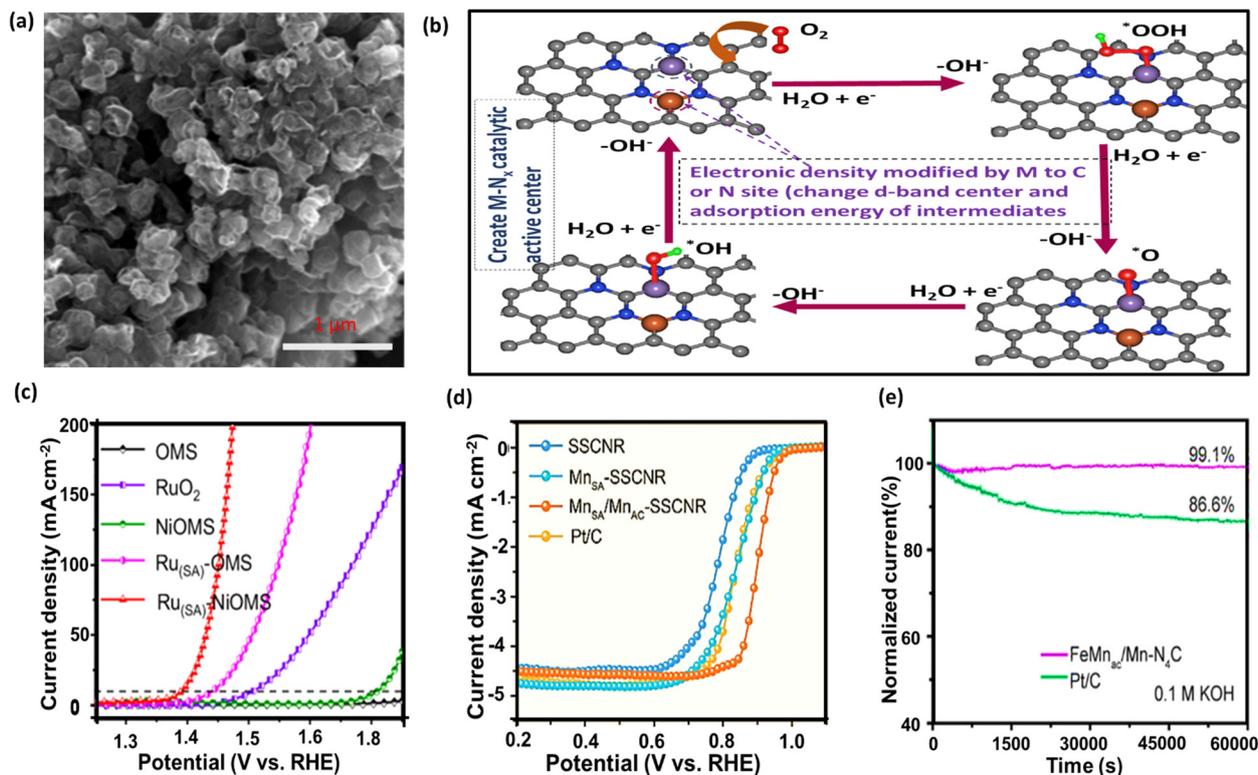
Fig. 5 (a) SEM image of a Mn–N@Gra-L single-atom-based catalyst. Reproduced from ref. 76 with permission from Elsevier, Copyright 2025, (b) Schematic illustration of adsorption and desorption mechanisms of reaction intermediates in Mn–Fe@N-doped CNT SAC and (c) LSV plot represents the performance of Mn-incorporated Ru$_{(SA)}$-OMS SACs for the OER. Reproduced from ref. 69 with permission from Tixin Hao *et al.*, Copyright© 2024, (d) LSV plot of Mn$_{SA}$/Mn$_{AC}$-SSCNR showing superior half-wave potential compared to Pt/C. Reproduced from ref. 75 with permission from John Wiley and Sons, copyright 2023, (e) Comparative durability (*i–t* plot) of SACs *versus* Pt/C over 60 000 s. Reproduced from ref. 82 with permission from John Wiley and Sons, copyright 2022.

overpotentials, high onset and half-wave potentials, robust four-electron transfer pathways, and long-term electrochemical stability (Fig. 6).

6. Mn-based LDHs, nitrides, and phosphorus derivatives

Following the discussion on oxides and MOFs, this section focuses on another important class of Mn-based electrocatalysts—LDHs, nitrides, and phosphorus derivatives—which are grouped based on their structural and compositional features that allow for efficient electronic structure modulation. Unlike simple oxides or molecular frameworks, these materials offer unique advantages such as layered structures (in LDHs), strong covalent bonding networks (in nitrides), and enhanced conductivity (in phosphides). This classification by material type enables us to systematically compare the role of Mn and related electronic regulation strategies across distinct structural platforms. Notably, the regulation of the d-band centre and e$_g$ orbital occupancy continues to be a central theme across these systems, influencing OER/ORR kinetics and stability.

LDHs composed of transition metals such as Ni, Co, Mn, and Fe, along with non-metal dopants, have garnered attention as promising OER/ORR electrocatalysts due to their layered structures, tunable compositions, and efficient charge transport capabilities.[96,97] A key strategy in improving their catalytic performance lies in electronic structure regulation, particularly through modulation of the d-band centre and e$_g$ orbital occupancy. These parameters influence the adsorption strength of reaction intermediates and, consequently, catalytic activity and stability.[50,98,99]

Shakeel *et al.* demonstrated that introducing Mn into a Ni–Mn-LDH/g-C$_3$N$_4$ composite enhances OER activity by increasing the density of active sites and fine-tuning the electronic configuration. The synergistic redox coupling between Ni^{2+}/Ni^{3+} and Mn^{3+}/Mn^{4+} promotes charge transfer, resulting in improved reaction kinetics—evident from a reduced overpotential (316 mV to 296 mV) and a lower Tafel slope (65 to 55 mV dec^{-1}).[100,101] The Mn incorporation also stabilizes the LDH structure and prevents aggregation, while the g-C$_3$N$_4$ support facilitates fast electron transfer and suppresses recombination, enhancing the overall electrocatalytic efficiency.

Building on this approach, Zhang *et al.* developed a hierarchical Mo$_4$C@g-C$_3$N$_4$@NiMn-LDH catalyst, in which Mn plays a pivotal role in stabilizing Ni^{3+} redox transitions and shifting the Ni^{3+} binding energy, thereby optimizing OH$^-$ adsorption and OER activity.[102] The core–shell architecture

17108 | *Phys. Chem. Chem. Phys.*, 2025, **27**, 17099–17115

This journal is © the Owner Societies 2025

integrates a conductive Mo_4C core and a g-C_3N_4 layer to ensure structural stability and efficient electron transport, while NiMn-LDH on the outer surface provides abundant active sites. Zhao *et al.* synthesized a bifunctional CoMn-LDH/N,P-GA catalyst (N,P co-doped graphene aerogel on CoMn-LDH), which surpasses the performance of Pt/C (ORR) and IrO_4 (OER) reference catalysts. The enhancement is attributed to improved surface area, low double-layer capacitance, and smaller Tafel slopes (73 *vs.* 106 mV dec^{-1}), indicating faster charge-transfer kinetics.[103] Defect engineering, especially the creation of oxygen vacancies, has also been shown to regulate the electronic structure effectively. For instance, Ov-NiMn-LDH/NCNTG (Fig. 5(c))—a catalyst comprising N-doped carbon nanotubes and N-doped graphene—exhibits enhanced ORR activity due to synergistic effects between oxygen vacancies and conductive carbon supports.[104]

Similarly, MnO_4/NiFe-LDH@$NiCo_4S_4$ shows outstanding OER performance (overpotential: 300 mV; Tafel slope: 42.43 mV dec^{-1}) and excellent stability over 10 days, owing to the core–shell structure and optimized electronic properties.[107] Furthermore, chemical reduction methods also offer promising strategies for tuning the electronic structure. In NiMn-LDHs, partial reduction *via* ethylene glycol generates surface oxygen vacancies that improve charge transfer and increase active site exposure. This leads to a measurable decrease in OER onset potential (from 1.47 V to 1.45 V), confirming the efficacy of this method.[104]

Phosphide-based Mn-containing catalysts also benefit from electronic tuning. A one-step electrodeposition technique produced a MnO_4/$Co_3(PO_4)_4$ catalyst with an OER overpotential of 225 mV at 10 mA cm^{-2} and good stability over 48 h.[108] Similarly, MnNiCoP/FeOOH, a 3D heterostructure synthesized *via* phosphorylation, demonstrates remarkable bifunctionality for the HER and OER, with a large double-layer capacitance (21.1 mF cm^{-2}) indicating a high surface area and enhanced catalytic efficiency.[109] Wang *et al.* further reported a Mn-doped Ni_4P/Cu_3P catalyst exhibiting outstanding kinetics (Tafel slope: 25.15 mV dec^{-1}; 10 mA cm^{-2} at 161 mV overpotential). Density functional theory (DFT) calculations confirmed that Mn–Ni_4P modulates water adsorption energy, while Cu_3P enhances conductivity, together optimizing the catalyst's electronic structure.[110] Overall, these findings underscore that tailoring the d-band centre and e_g orbital occupancy *via* heteroatom doping, defect engineering, and interfacial modulation significantly enhances Mn-based catalyst performance for the OER/ORR. The ability to precisely tune these electronic parameters is central to the development of next-generation bifunctional electrocatalysts.[106,111,112]

7. Challenges and mechanistic solutions for Mn-based electrocatalysts and summary

Despite the promising activity of Mn-based electrocatalysts, several persistent challenges—spanning from material synthesis to operational durability—limit their scalability and commercial viability. For example, Mn oxides, though abundant and cost-effective, suffer from poor electrical conductivity and limited long-term stability, especially under harsh alkaline or acidic conditions. Simple MnO_x phases often degrade under prolonged operation, whereas spinel and perovskite structures (*e.g.*, Mn_3O, $LaMnO_3$) offer better crystallinity and tunable oxygen vacancies. However, achieving optimal e_g orbital occupancy and surface reactivity for both high activity and stability remains challenging.[113,114] To address poor conductivity, incorporating conductive supports such as carbon nanotubes or graphene, or hybridizing with other metal oxides (*e.g.*, Co_3O_4 or ZnO), can significantly enhance charge transfer and introduce synergistic effects that improve both catalytic activity and stability. For instance, the incorporation of reduced graphene oxide (rGO) into Co_4FeO_4 to form a Co_4FeO_4@rGO hybrid material has been shown to enhance conductivity, create abundant oxygen vacancies, and introduce favourable mixed valence states, leading to improved trifunctional activity and durability.[115,116] Defect engineering, such as introducing oxygen vacancies or heteroatom doping, can further optimize the electronic structure and enhance performance as summarized in Table 1.[62,64,117,118]

Mn-based MOFs, despite their high surface area and porosity, exhibit poor intrinsic conductivity and are structurally vulnerable during cycling. Similarly, Mn-containing layered double hydroxides (LDHs) often show sluggish charge transfer and low conductivity, with risks of delamination or irreversible reconstruction under OER/ORR conditions. Hybridizing these materials with conductive substrates or nanoparticles, and employing robust, electrochemically stable linkers, can enhance both conductivity and durability.[70,129] In particular, the combination of Mn with Fe or Co in MOF frameworks or derived composites can modulate the local electronic structure, reduce energy barriers for intermediate adsorption/desorption, and facilitate lattice oxygen participation, improving both activity and stability.[115]

For Mn SACs, achieving uniform dispersion and preventing agglomeration is difficult, and their activity is highly sensitive to the coordination environment (*e.g.*, Mn–N_4 or Mn–O_4), which is challenging to control at scale. Using defect-rich or heteroatom-doped carbon supports, and *in situ* synthesis techniques, can help stabilize single Mn atoms and control their local environment, while modulation of the coordination environment beyond the first shell can further optimize activity and stability.[130] The concept of stabilizing noble metal atoms on 2D substrates, such as Pd on MoS_4 *via* UV-assisted reduction, demonstrates how defect engineering and strong metal–support interactions can maintain atomic dispersion and significantly lower charge transfer resistance. These design principles can be adapted to Mn SAC systems to achieve similar stabilization and enhanced performance.[131]

In addition, Mn-based nitrides and phosphides, while offering better conductivity, are prone to surface oxidation, leading to passivation layers and potential Mn leaching. Their frameworks may also degrade in alkaline environments, limiting
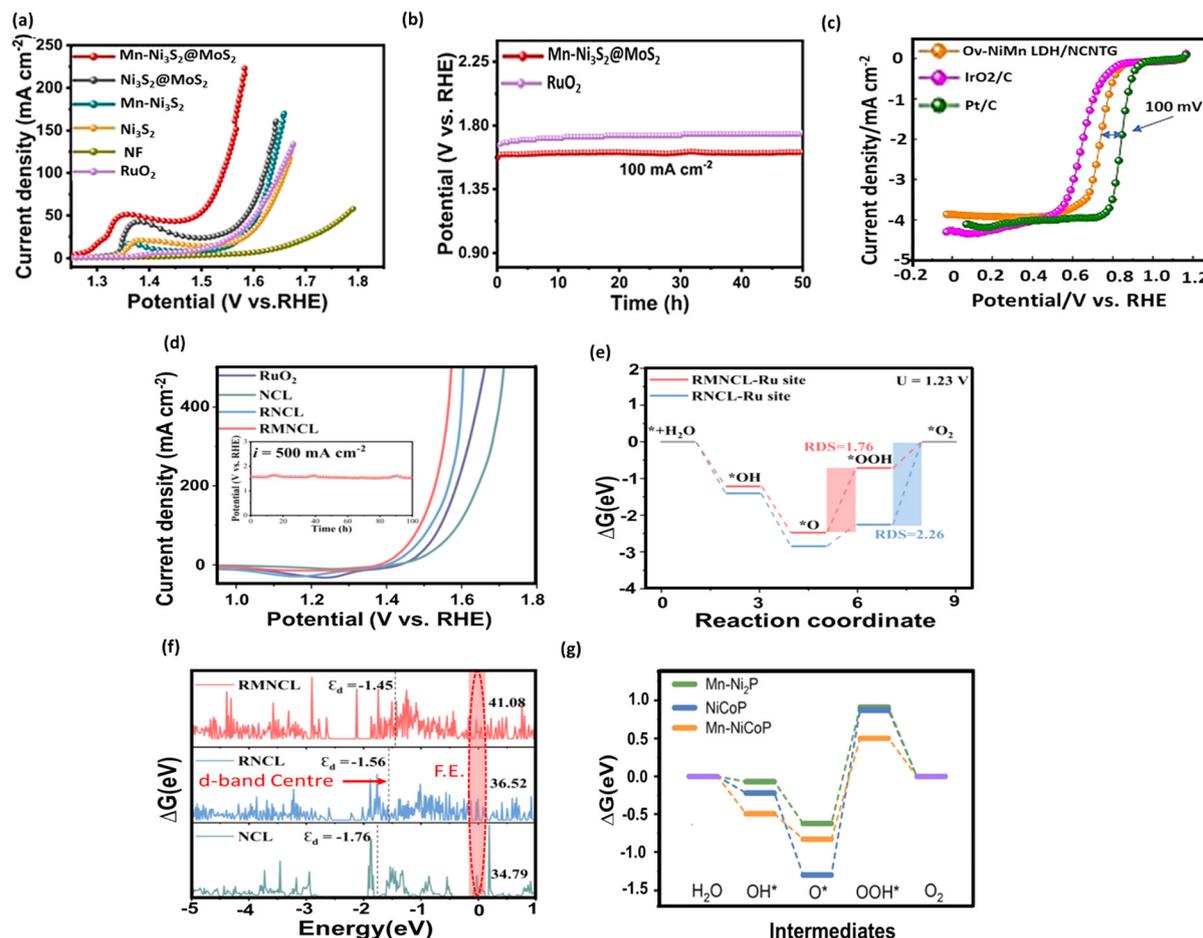
This journal is © the Owner Societies 2025

Phys. Chem. Chem. Phys., 2025, **27**, 17099–17115 | **17109**

Fig. 6 (a) LSV plot of the Mn−Ni$_3$S$_4$@MoS$_4$ composite compared to the benchmark RuO$_4$ catalyst and various counterparts. Reproduced from ref. 92 with permission from American Chemical Society, copyright© 2024, (b) durability performance of Mn−Ni$_3$S$_4$@MoS$_4$ and RuO$_4$ at a current density of 100 mA cm^{-2}. Reproduced from ref. 92 with permission from American Chemical Society, copyright© 2024, (c) comparative ORR performance of oxygen vacancy-engineered O$_v$-NiMn LDH/NCNTG with standard catalysts IrO$_4$/C and Pt/C. Reproduced from ref. 104 with permission from Elsevier copyright 2024, (d) LSV curve of Ru, Mn co-doped NiCo−LDH compared with RuO$_4$ for the OER, demonstrating high durability at 500 mA cm^{-2}. Reproduced from ref. 105 with permission from Elsevier, copyright 2024, (e) Free energy diagrams showing improved OER kinetics and reduced RDS energy barrier after Mn doping. Reproduced from ref. 105 with permission from Elsevier, copyright 2024, (f) d-band centre (ε$_d$) values shift closer to the Fermi level from NCL (−1.76 eV) to RMNCL (−1.45 eV), indicating improved electronic interactions and OER activity after Ru and Mn doping. Reproduced from ref. 105 with permission from Elsevier, copyright 2024, (g) Free energy diagram showing reduced *OH → *O and *O → O$_4$ barriers after Mn doping. Reproduced from ref. 106 with permission from Elsevier, copyright 2023.

durability. Surface passivation control and alloying with secondary metals (*e.g.*, Fe, Co, Ni, Cu, and Ag) can enhance structural robustness and suppress leaching, as supported by DFT studies showing that partial substitution at the Mn site improves electronic conductivity and stability.[132] The integration of rGO into bimetallic oxide composites (*e.g.*, Co$_4$FeO$_4$@rGO) not only improves electrical conductivity but also stabilizes multivalent states of Co and Fe, which can be strategically applied to stabilize Mn-based nitride and phosphide systems.[115]

Mn chalcogenides (sulfides, selenides, and tellurides) tend to transform into amorphous (oxy)hydroxide layers during catalysis. While this surface reconstruction can sometimes be beneficial, uncontrolled phase changes and dissolution in alkaline media remain critical issues. Designing catalysts for controlled surface reconstruction and introducing stabilizing

additives or dopants can help maintain structural integrity during operation. For example, Pd NPs incorporated onto MoS$_4$ nanosheets *via* UV-assisted methods have been shown to enhance OER activity by lowering the overpotential to 253 mV and reducing the Tafel slope to 59 mV dec^{-1}, while maintaining structural integrity and conductivity—demonstrating the benefits of synergistic interactions and surface modulation.[131] These approaches can inform the development of stable Mn-based chalcogenide systems.

Finally, achieving high intrinsic activity and selectivity for the OER/ORR is limited by the difficulty in optimizing the active site structure and electronic configuration, especially in complex or multi-metal systems. Theoretical calculations and targeted doping (*e.g.*, Cr, Fe, and Ni) can modulate the oxidation state and local environment of Mn, enhancing per-site activity and selectivity, while atomic-level design and advanced

17110 | *Phys. Chem. Chem. Phys.*, 2025, **27**, 17099–17115

This journal is © the Owner Societies 2025

Table 1 Comprehensive comparison of material composition, modification strategies, electronic structures, oxygen vacancy formation, Mn–O bond covalency, mechanistic insights, performance metrics, and durability for Mn-based catalysts

Material composition	Modification strategy	e_g orbital occupation effect	Oxygen vacancy formation energy	Mn–O bond covalency impact	Performance improvement/mechanistic insight	Performance metrics	Durability	Ref.
Mn–Co$_3$O$_4$	Mn/Co ratio tuning, defect engineering	Optimized e_g occupancy for the OER	Lowered by oxygen vacancy engineering	Increased covalency, better charge transfer	Enhanced OER activity via more active sites and improved electron transfer	η_{10} = 265 mV, Tafel = 76.8 mV dec^{-1}	100 h@10 mA cm^{-2}	49
(Ni, Mn)–ZnO/g-C$_3$N$_4$	Mn doping, defect engineering	e_g tuning via Mn doping	Increased oxygen vacancies	Improved covalency	Improved OER via more active sites and enhanced conductivity	η_{10} = 338 mV, Tafel = 72 mV dec^{-1}	—	100
Mn–Co$_3$O$_4$-200	Oxygen vacancy engineering	e_g occupancy optimized by vacancies	Substantially reduced	Strengthened Mn–O bond	High OER activity attributed to the increased surface area and active site exposure	η_{10} = 270 mV@20 mA cm^{-2}, C_{dl} = 10.7, Tafel = 46.9	160 h, 98% retention	119
NiMoS/NiFeMn-LDH	Multi-metal doping, defect engineering	Synergistic e_g tuning	Facilitated by multi-metal defects	Enhanced covalency, multi-metal synergy	Lowered overpotential and improved kinetics due to synergistic effects	η_{10} = 192 mV, C_{dl} = 9.18, Tafel = 30.3	50 h	120
Mn–FeTiO$_3$	Mn doping, defect engineering	e_g occupancy tuned for optimal adsorption	Increased vacancy concentration	Improved covalency	Enhanced OER by increased active sites and conductivity	η_{10} = 190 mV, Tafel = 32 mV dec^{-1}	40 h	55
Mn–Ni$_3$Se$_4$@NF	Mn doping, defect engineering	e_g tuning via Mn incorporation	More oxygen vacancies	Improved Mn–Se covalency	Boosted OER/ORR activity via higher conductivity and more active sites	η = 1.66 V@100 mA cm^{-2}, Tafel = 128.9 mV dec^{-1}	56 h	121
MnO$_4$/Co$_3$(PO$_4$)$_4$	Mn/Co synergy, phosphate stabilization	e_g occupancy tuned by Mn/Co ratio	Phosphate stabilizes vacancies	Enhanced covalency	Dual-site catalysis, improved OER/ORR due to stabilized active sites	η_{10} = 225 mV, η_{50} = 310 mV, C_{dl} = 3.98, Tafel = 44.81 mV dec^{-1}	48 h@100/10 mA cm^{-2}, 94/96% retention	108
MnNiCoP/FeOOH	Multi-metal doping, defect engineering	Synergistic e_g tuning	Facilitated vacancy creation	Stronger covalency, improved charge transfer	Enhanced bifunctional activity and stability	η_{10} = 251 mV@100 mA cm^{-2}, C_{dl} = 21.1, Tafel = 65.1 mV dec^{-1}	80 h@50 mA cm^{-2}	109
Mn-doped Ni$_4$P/Cu$_3$P	Mn doping, defect engineering	e_g tuning via Mn doping	Lowered vacancy formation energy	Enhanced Mn–P covalency	Efficient seawater electrolysis, improved HER/OER by optimized electronic structure	η_{10} = 161 mV, C_{dl} = 9.58, Tafel = 25.15 mV dec^{-1}	12 h	110
FeCoNiMn-MOF/NF	Multi-metal doping, MOF structure	Synergistic e_g tuning	Increased vacancy concentration	Enhanced covalency, porous structure	Improved electron transfer, high surface area, and bifunctional activity	η_{50} = 239 mV, C_{dl} = 5.36, Tafel = 62.05 mV dec^{-1}	100 h	122
MnTe@MnO	Heterostructure formation	e_g tuning at the Mn–O/Te interface	Increased vacancies at the interface	Strengthened interface covalency	Enhanced OER/ORR via a heterojunction effect	η_{10} = 208 mV, C_{dl} = 4, Tafel = 39 mV dec^{-1}	50 h	123
NiSe/MnTe	Mn/Te synergy, defect engineering	e_g tuning by dual metal synergy	Facilitated vacancy formation	Enhanced covalency	Improved OER/ORR by the synergistic effect	η_{10} = 170 mV, Tafel = 32 mV dec^{-1}	60 h	124
10% Mn-doped FeSe$_4$	Mn doping, defect engineering	e_g occupancy optimized by Mn	Increased vacancy concentration	Improved covalency	Enhanced OER by increased conductivity and active sites	η_{10} = 133 mV	30 h	87
Mn-doped ZnO NPs	Mn doping, defect engineering	e_g tuning via Mn doping	Increased oxygen vacancies	Improved covalency	Enhanced ORR by more active sites and improved electron transfer	$E_{1/4}$ = 1.16 V, E_{onset} = 1.56 V	800 s	117
(Co$_{0.95}$Mn$_{0.05}$)$_4$P@NC	Mn/Co synergy, defect engineering	e_g tuning by Mn/Co synergy	Facilitated vacancy formation	Improved covalency	Enhanced ORR, high stability	E_{onset} = 0.90 V, $E_{1/4}$ = 0.86 V, Tafel = 46 mV dec^{-1}	92% retention after 10 h	125
Mn-doped Ni-MOF	Mn doping, defect engineering	e_g tuning via Mn doping	Increased oxygen vacancies	Improved covalency	Enhanced ORR, improved electron transfer	E_{onset} = 0.83 V, $E_{1/4}$ = 0.74 V, Tafel = 64.21 mV dec^{-1}	2000 cycles	64

This journal is © the Owner Societies 2025

Phys. Chem. Chem. Phys., 2025, **27**, 17099–17115 | 17111

Table 1 (continued)

Material composition	Modification strategy	e_g orbital occupation effect	Oxygen vacancy formation energy	Mn–O bond covalency impact	Performance improvement/mechanistic insight	Performance metrics	Durability	Ref.
Fe/Mn-SNC	Fe/Mn Co-doping, defect engineering	e_g tuning by Fe/Mn synergy	Increased vacancy concentration	Enhanced covalency	Improved ORR, high durability	E_{onset} = 0.98 V, $E_{1/4}$ = 0.92 V, Tafel = 65.5 mV dec^{-1}	68.56% after 50 000 s CP	126
LaMn$_{0.3}$Co$_{0.7}$-O$_{3-\delta}$ (Perovskite)	Mn/Co synergy, oxygen deficiency	e_g tuning by Mn/Co ratio	Oxygen-deficient structure	Improved covalency	Enhanced ORR/OER via higher conductivity and more active sites	E_{onset} = 0.79 V, $E_{1/4}$ = 0.56 V, Tafel = 111 mV dec^{-1}	71.8% retention at 20 h	56
MOF-derived Mn/Co-C-N (1:2)	Mn/Co synergy, defect engineering	e_g tuning by dual metal synergy	Increased vacancy concentration	Improved covalency	Improved ORR, high cycling stability	$E_{1/4}$ = 0.80 V, Tafel = 60 mV dec^{-1}	8 mV decline after 10 000 cycles	65
Ag-Mn (nanoporous)	Mn/Ag interface, defect engineering	e_g tuning at the interface	Increased vacancy concentration	Improved covalency	Enhanced ORR by the synergistic interface effect	$E_{1/4}$ = 0.81 V, Tafel = 57.75 mV dec^{-1}	10 mV decline after 5000 cycles	127
(Mn-N-C)	Mn–N–C active site engineering	e_g tuning at Mn–N–C sites	Increased vacancy concentration	High covalency at N–C sites	Improved ORR, high durability	$E_{1/4}$ = 0.90 V, Tafel = 56.96 mV dec^{-1}	8 mV decline after 5000 cycles	128
Zn$_{0.4}$Co$_{0.8}$Mn$_4$O$_4$/CNT	Mn/Co synergy, defect engineering	e_g tuning by Mn/Co synergy	Increased vacancy concentration	Improved covalency	Enhanced ORR, high current retention	$E_{1/4}$ = 0.81 V, Tafel = 66.75 mV dec^{-1}	92.5% retention after 20 000 cycles	51

characterization enable fine-tuning of the electronic and geometric structure at the atomic scale.[133] However, these mechanistic strategies have been successfully demonstrated in recent studies on Mn-based materials and transition metal oxide composites. Applying them systematically can help overcome the main challenges faced by Mn-based electrocatalysts.

This article provides a comprehensive review of manganese-based (Mn-based) noble metal-free electrocatalysts, detailing their structural diversity, synthesis methodologies, and mechanistic advantages for the OER and ORR. It systematically categorizes Mn-based materials—such as oxides, chalcogenides, phosphides, nitrides, layered double hydroxides, metal–organic frameworks, and single-atom catalysts—highlighting how their tunable redox states, defect engineering, and heteroatom doping strategies contribute to improved catalytic efficiency, conductivity, and stability. The review emphasizes the importance of electronic structure modulation, particularly through d-band centre tuning and e_g orbital occupancy, to optimize intermediate adsorption and reaction kinetics. It also contrasts the performance enhancements achieved by compositional control, hybridization with conductive supports, and interfacial engineering. Persistent challenges, including conductivity limitations, phase instability, and catalyst degradation, are addressed alongside proposed solutions such as advanced doping, defect creation, and hybrid material design. The article concludes by underscoring the need for precise electronic and structural control to realize the full potential of Mn-based catalysts in next-generation sustainable energy technologies.

Author contributions

A. B.: analysed the data and wrote the manuscript. S. P.: supervised and revised the manuscript.

Conflicts of interest

There are no conflicts to declare.

Data availability

No new data were generated in this study. All data cited are available in the referenced publications.

Acknowledgements

Notes and references

1 L. Mu, J. Ying, Y. Ou, Z. Wang, Y. Liu, N. Zhao, M. Xue, Y. Dai and G. Zhao, *J. Colloid Interface Sci.*, 2025, **688**, 106–117.

17112 | *Phys. Chem. Chem. Phys.*, 2025, **27**, 17099–17115

This journal is © the Owner Societies 2025

2 I. Fareed, M. D. Khan, S. Murtaza, M. ul Hassan Farooq, Z. U. Rehman, M. U. Farooq, F. K. Butt and M. Tahir, *RSC Adv.*, 2024, **14**, 26556–26567.

3 W. Li, R. Liu, G. Yu, X. Chen, S. Yan, S. Ren, J. Chen, W. Chen, C. Wang and X. Lu, *Small*, 2024, **20**, 2307164.

4 Z. Xiao, F. Hou, X. Zhang, L. Pan, J. J. Zou and G. Li, *Langmuir*, 2024, **40**, 10561–10570.

5 J. Woo, S. Han and J. Yoon, *ACS Appl. Mater. Interfaces*, 2024, **16**, 23288–23295.

6 X. Chai, X. Du and X. Zhang, *Fuel*, 2024, **377**, 132781.

7 M. Yang, X. Wang, X. Xu, Y. Li, Y. Liu and J. Zhao, *J. Mater. Sci. Technol.*, 2025, **211**, 123–133.

8 Y. Zeng, X. Tan, Z. Zhuang, C. Chen and Q. Peng, *Angew. Chem., Int. Ed.*, 2025, **137**(4), 202416715.

9 H. Zhao, L. Zhu, J. Yin, J. Jin, X. Du, L. Tan, Y. Peng, P. Xi and C. H. Yan, *Angew. Chem., Int. Ed.*, 2024, **63**, 202402171.

10 M. R. Kandel, U. N. Pan, P. P. Dhakal, R. B. Ghising, S. Sidra, D. H. Kim, N. H. Kim and J. H. Lee, *Small*, 2024, **20**, 2307241.

11 M. Z. Iqbal, M. Shaheen, U. Aftab, Z. Ahmad, M. Y. Solangi, M. I. Abro and S. M. Wabaidur, *Energy Fuels*, 2024, **38**, 2416–2425.

12 J. Lin, Y. Ding, H. Jin and T. Zeng, *Ionics*, 2024, **30**, 2287–2298.

13 H. He, T. Matsuda, A. Miura, M. Nagao, J. K. Padarti, T. Ohno and S. Hirai, *Sustainable Energy Fuels*, 2024, **8**, 789–796.

14 H. M. Zhang, J. Li, Y. Gao, J. Sun, S. Geng and Y. Meng, *Fuel*, 2024, **371**, 132111.

15 S.-C. Huang, Y.-L. Zhou, L. Duan, D.-Z. Luo, B.-P. Yang, G. Chen, X.-H. Liu, J.-G. Tang and N. Zhang, *Rare Met.*, 2025, **44**(2), 1042–1052.

16 A. Soundarya Mary, C. Murugan, D. Mahendiran, P. Murugan and A. Pandikumar, *Mater. Today Energy*, 2024, **41**, 101541.

17 M. Varničívarničíc, M. M. Pavlovícpavlović, S. Eraković, E. Pantovícpantović, M. Mihailovícmihailović, M. R. Pantović, P. Pavlovícpavlović, S. Srécko, S. Stopíc and B. Friedrich, *Metals*, 2022, **12**, 22.

18 R. Cheng, K. Li, H. Li, F. Sun, X. He, T. Zhao, J. Zhang and C. Fu, *Nano Res.*, 2024, **17**, 3622–3632.

19 K. Selvakumar, V. Duraisamy, S. Venkateshwaran, N. Arumugam, A. I. Almansour, Y. Wang, T. Xiaoteng Liu and S. Murugesan Senthil Kumar, *ChemElectroChem*, 2022, **9**, 202101303.

20 Z. Zeng, S. Kuang, Z. F. Huang, X. Chen, Y. Su, Y. Wang, S. Zhang and X. Ma, *Chem. Eng. J.*, 2022, **433**, 134446.

21 Y. J. Sa, S. Kim, Y. Lee, J. M. Kim and S. H. Joo, *ACS Appl. Mater. Interfaces*, 2023, **15**, 31393–31402.

22 Y. Pei, D. P. Wilkinson and E. Gyenge, *Small*, 2023, **19**, 2204585.

23 G. Yusibova, J. M. Assafrei, K. Ping, J. Aruväli, P. Paiste, M. Käärik, J. Leis, H. M. Piirsoo, A. Tamm, A. Kikas, V. Kisand, P. Starkov and N. Kongi, *J. Electroanal. Chem.*, 2023, **930**, 117161.

24 N. C. Maile, M. Moztahida, A. A. Ghani, M. Hussain, K. Tahir, B. Kim, S. K. Shinde, V. J. Fulari and D. S. Lee, *Chem. Eng. J.*, 2021, **421**, 129767.

25 S. Bhowmick, A. Dhankhar, T. K. Sahu, R. Jena, D. Gogoi, N. R. Peela, S. Ardo and M. Qureshi, *ACS Appl. Energy Mater.*, 2020, **3**, 1279–1285.

26 X. Dong, Y. Wang, J. Wang, Y. Sun, B. Xu, C. Li and L. Hang, *Int. J. Hydrogen Energy*, 2024, **73**, 558–565.

27 K. Li, Z. Dong and Z. Lü, *Electrochim. Acta*, 2022, **430**, 141123.

28 J. Sun, L. Du, B. Sun, G. Han, Y. Ma, J. Wang, H. Huo, P. Zuo, C. Du and G. Yin, *J. Energy Chem.*, 2021, **54**, 217–224.

29 C. Chowde Gowda, A. Mathur, A. Parui, P. Kumbhakar, P. Pandey, S. Sharma, A. Chandra, A. K. Singh, A. Halder and C. S. Tiwary, *J. Ind. Eng. Chem.*, 2022, **113**, 153–160.

30 Z. Hu, T. Shen, X. Chen, Z. Yan, T. Pan and H. Yu, *Prog. Nat. Sci.: Mater. Int.*, 2023, **33**, 328–334.

31 Y. Liu, L. Bai, T. Li, J. Huo, X. Wang, L. Zhang, X. Hao and S. Guo, *Appl. Surf. Sci.*, 2022, **577**, 151952.

32 S. Mondal, S. Sarkar, M. Riyaz, M. Kar, A. C. Fortuin, S. Vashishth, R. Das, M. Eswaramoorthy, D. Kramer and S. C. Peter, *ACS Energy Lett.*, 2024, **9**, 3440–3447.

33 Y. Xiong, Y. Yang, X. Feng, F. J. Disalvo and H. D. Abruña, *J. Am. Chem. Soc.*, 2019, **141**, 4412–4421.

34 A. Ali, N. Iqbal, T. Noor and U. Imtiaz, *J. Electroanal. Chem.*, 2022, **914**, 116324.

35 J. H. Siow, M. R. Bilad, W. Caesarendra, J. J. Leam, M. A. Bustam, N. S. Sambudi, Y. Wibisono and T. M. I. Mahlia, *Energies*, 2021, **14**(19), 6385.

36 M. M. Aslam, T. Noor, E. Pervaiz, N. Iqbal and N. Zaman, *Int. J. Hydrogen Energy*, 2024, **70**, 614–628.

37 W. Jin, P. Sharma, P. Singh, A. Kundu, G. Balasubramanian and H. M. Chan, *Metall. Mater. Trans. A*, 2024, **55**, 3799–3808.

38 J. Wang and Q. Yang, *Solid State Ionics*, 2024, **417**, 116691.

39 Z. Wang, L. Ai, P. Zhu, J. Zhao, B. Li, X. Duan and F. Yu, *J. Alloys Compd.*, 2022, **922**, 166237.

40 J. Chen, A. Gutierrez, M. A. Sultanov, J. Wen, J. R. Croy, Y. Wang, V. Srinivasan and P. Barai, *ACS Appl. Energy Mater.*, 2024, **7**, 2167–2177.

41 J. Dai, X. Li, Z. Sun, T. Chen, J. Wang and S. Zheng, *J. Colloid Interface Sci.*, 2025, **690**, 137305.

42 X. Ma, L. Schröck, G. Gao, Q. Ai, M. Zarrabeitia, C. Liang, M. Z. Hussain, R. Khare, K. T. Song, D. J. Zheng, M. Koch, I. E. L. Stephens, S. Hou, Y. Shao-Horn, J. Warnan, A. S. Bandarenka and R. A. Fischer, *ACS Catal.*, 2024, **14**, 15916–15926.

43 D. Zhang, F. She, J. Chen, L. Wei and H. Li, *J. Am. Chem. Soc.*, 2025, **147**, 6076–6086.

44 L. Huo, M. Lv, M. Li, X. Ni, J. Guan, J. Liu, S. Mei, Y. Yang, M. Zhu, Q. Feng, P. Geng, J. Hou, N. Huang, W. Liu, X. Y. Kong, Y. Zheng and L. Ye, *Adv. Mater.*, 2024, **36**, 2312868.

45 H. B. M. Sidek, J. Lee, X. Jin and S. J. Hwang, *Bull. Korean Chem. Soc.*, 2023, **44**, 962–968.

46 X. He, T. Qiao, B. Li, Z. Zhang, S. Wang, X. Wang and H. Liu, *ChemElectroChem*, 2023, **10**, 202200933.

47 L. Zhang, B. Lin, S. Ye, S. Chen, Z. Yao, J. Lin, X. Lin, C. Guo, J. He, Y. Chen, Y. Liu, Z. Tang, L. Shen, X. Li, S. Nie, B. Lan, H. Liang and X. Luo, *J. Alloys Compd.*, 2023, **956**, 170218.

48 A. Vazhayil, S. Ashok C and N. Thomas, *J. Electroanal. Chem.*, 2023, **934**, 117298.

49 L. Zhang, F. Wei and H. Liang, *Mater. Today Commun.*, 2024, **40**, 109887.

50 H. J. Liu, S. Zhang, R. Y. Fan, B. Liu, R. Q. Lv, Y. M. Chai and B. Dong, *Appl. Catal., B*, 2024, **343**, 123567.

51 H. Kang, Y. Liu, M. Wei, L. Zhou and C. Wang, *J. Alloys Compd.*, 2024, **1000**, 175089.

52 M. Wang, H. Du, H. Zhao, Y. Cao, R. Dong, H. Wang and H. Hou, *ACS Sustainable Chem. Eng.*, 2023, **11**, 9478–9488.

53 X. Zhang, Q. Liu, S. Liu and E. Wang, *Electrochim. Acta*, 2023, **437**, 141477.

54 P. V. Ambeth, M. H. Ahmed and M. Konarova, *ChemCatChem*, 2025, 202401980.

55 K. Ashfaq, G. A. M. Mersal, A. M. Fallatah, M. M. Ibrahim, A. Kumar and Z. M. El-Bahy, *JOM*, 2024, **77**, 2025.

56 X. Y. Gao, H. Liu, Y. Wang, J. H. Guo, X. W. Sun, W. Y. Sun, H. Zhao, J. Bai and C. P. Li, *J. Colloid Interface Sci.*, 2023, **650**, 951–960.

57 Y. Ye, L. Zhang, Q. Zhu, Z. Du, T. Wågberg and G. Hu, *J. Colloid Interface Sci.*, 2023, **650**, 1350–1360.

58 L. Zhang, D. Huan, K. Zhu, P. Dai, R. Peng and C. Xia, *ACS Appl. Mater. Interfaces*, 2022, **14**, 17358–17368.

59 J. X. Flores-Lasluisa, F. Huerta, D. Cazorla-Amorós and E. Morallón, *Energy*, 2022, **247**, 123456.

60 G. Dey, R. Jana, S. Saifi, R. Kumar, D. Bhattacharyya, A. Datta, A. S. K. Sinha and A. Aijaz, *ACS Nano*, 2023, **17**, 19155–19167.

61 W. Luo, L. Cao, M. Hou, Y. Zhou, Z. Ren, J. Geng and Z. Shao, *Int. J. Energy Res.*, 2023, **2023**, 9148994.

62 S. Mao, L. Ye, S. Jin, C. Zhou, J. Pang and W. Xu, *Inorg. Chem.*, 2024, **63**, 6005–6015.

63 S. Saha, A. De, S. Banerjee, A. K. Das, C. A. Ohlin and R. Mondal, *Inorg. Chem.*, 2024, **63**, 10619–10633.

64 N. Iqbal, R. Ahmad, T. Noor, N. Shahzad and M. I. Shahzad, *Mater. Chem. Phys.*, 2025, **334**, 130448.

65 Y. Qiao, Y. Guo, Y. Zhao, C. Chang, S. Wang, X. Zhang, F. Gao, R. Chen and L. Hou, *Nanotechnology*, 2024, **36**, 035703.

66 S. Li, Z. Wang, Y. Yang, S. Pan, W. Pan, M. Tang and K. Liu, *J. Electroanal. Chem.*, 2024, **970**, 118553.

67 T. Zhang, B. Zhang, Q. Peng, J. Zhou and Z. Sun, *J. Mater. Chem. A*, 2021, **9**, 433–441.

68 H. Seong and D. Lee, *Bull. Korean Chem. Soc.*, 2024, **45**, 435–450.

69 Y. Hao, S.-F. Hung, L. Wang, L. Deng, W.-J. Zeng, C. Zhang, Z.-Y. Lin, C.-H. Kuo, Y. Wang, Y. Zhang, H.-Y. Chen, F. Hu, L. Li and S. Peng, *Nat. Commun.*, 2024, **15**, 8015.

70 G. Zhong, L. Zou, X. Chi, Z. Meng, Z. Chen, T. Li, Y. Huang, X. Fu, W. Liao, S. Zheng, Y. Xu, F. Peng and X. Peng, *Carbon Energy*, 2024, **6**, 484.

71 W. Lee, J. Kim, H. Kim and S. Back, *Phys. Chem. Chem. Phys.*, 2022, **24**, 19911–19918.

72 L. Ran, Y. Xu, X. Zhu, S. Chen and X. Qiu, *ACS Nano*, 2024, **18**, 750–760.

73 X. Wei, S. Song, W. Cai, Y. Kang, Q. Fang, L. Ling, Y. Zhao, Z. Wu, X. Song, X. Xu, S. M. Osman, W. Song, T. Asahi, Y. Yamauchi and C. Zhu, *ACS Nano*, 2024, **18**, 4308–4319.

74 L. Gong, J. Zhu, F. Xia, Y. Zhang, W. Shi, L. Chen, J. Yu, J. Wu and S. Mu, *ACS Catal.*, 2023, **13**, 4012–4020.

75 Y. Li, Z. Li, K. Shi, L. Luo, H. Jiang, Y. He, Y. Zhao, J. He, L. Lin, Z. Sun and G. Sun, *Small*, 2024, **20**, 2309727.

76 H. Chen, C. Xu, L. Sun, C. Guo, H. Chen, C. Shu, Y. Si, Y. Liu and R. Jin, *J. Colloid Interface Sci.*, 2024, **673**, 239–248.

77 G. Chao, Y. Zhang, L. Zhang, W. Zong, N. Zhang, T. Xue, W. Fan, T. Liu and Y. Xie, *J. Mater. Chem. A*, 2021, **10**, 5930–5936.

78 J. Bai, Y. Fu, P. Zhou, P. Xu, L. Wang, J. Zhang, X. Jiang, Q. Zhou and Y. Deng, *ACS Appl. Mater. Interfaces*, 2022, **14**, 29986–29992.

79 L. Yan, L. Xie, X. L. Wu, M. Qian, J. Chen, Y. Zhong and Y. Hu, *Carbon Energy*, 2021, **3**, 856–865.

80 M. Tong, F. Sun, G. Xing, C. Tian, L. Wang and H. Fu, *Angew. Chem., Int. Ed.*, 2023, **62**(52), 202314933.

81 P. Li, C. Zhu, L. Yang, J. Shi, W. Hu, Z. Li, J. Wu and H. Wang, *Energy Storage Mater.*, 2024, **71**, 103639.

82 H. Liu, L. Jiang, J. Khan, X. Wang, J. Xiao, H. Zhang, H. Xie, L. Li, S. Wang and L. Han, *Angew. Chem., Int. Ed.*, 2023, **135**, 202214988.

83 Z. M. Almarhoon, K. Jabbour, S. Manzoor, S. I. A. Shah, M. F. Ashiq, M. Y. Ur Rehman, M. F. Ehsan, M. Najam-ul-Haq and M. N. Ashiq, *Fuel*, 2024, **363**, 130919.

84 Y. Chen, H. Wu, N. Tang, Y. Zhang and Y. Wang, *Chem. Commun.*, 2024, **60**, 1751–1753.

85 S. Wang, Y. Zhang and J. Wang, *Energy Fuels*, 2024, **38**, 19038–19047.

86 Y. R. Rosyara, A. Muthurasu, K. Chhetri, I. Pathak, T. H. Ko, P. C. Lohani, D. Acharya, T. Kim, D. Lee and H. Y. Kim, *ACS Appl. Mater. Interfaces*, 2024, **16**, 10238–10250.

87 H. A. Alburaih, M. Z. Ansari, A. G. Abid, R. Y. Khosa, M. N. Ashiq, S. Manzoor, S. Aman, H. Chaudhry, M. S. Waheed and T. A. Taha, *J. Sol-Gel Sci. Technol.*, 2023, **106**, 1–9.

88 P. Rani, R. Biswas, A. Dutta and P. S. Alegaonkar, *Energy Fuels*, 2024, **38**, 16809–16819.

89 M. Sadaqat, S. Manzoor, S. Aman, S. Gouadria, M. Usman, K. S. Joya, M. Najam-Ul-Haq, H. M. A. Hassan, M. N. Ashiq and T. A. Taha, *Energy Fuels*, 2022, **36**, 10327–10338.

90 X. Yu, X. Chen, D. Yue, F. Zheng, Q. Li, Z. Ma and H. Wang, *J. Alloys Compd.*, 2024, **1005**, 176153.

91 X.-Q. Wang, X.-Y. Ma, W.-Z. Wu, H.-B. He, N.-N. Wang, R.-J. Zheng, S.-J. Ma, Y.-Q. Zhu, P.-K. Shen and J.-L. Zhu, *Rare Met.*, 2024, **43**(5), 1977–1988.

92 S. Ye, Z. Du, Z. Cai, D. Ou, H. Guo, Q. Liu, W. Yang and Q. Shi, *ACS Appl. Nano Mater.*, 2024, **7**, 3096–3104.

17114 | *Phys. Chem. Chem. Phys.*, 2025, **27**, 17099–17115

This journal is © the Owner Societies 2025

93 A. Maheen, S. A. Alsalhi, K. Tahir, A. Kumar, R. S. K. Sharma, P. K. Pathak, S. Saini, V. K. Pandey and R. Haldhar, *J. Sol-Gel Sci. Technol.*, 2025, **114**, 496–507.

94 N. Rasool, H. A. Alyousef, A. W. Alrowaily, B. M. Alotaibi, A. G. Al-Sehemi and K. Ahmad, *J. Korean Ceram. Soc.*, 2025, **62**, 46–55.

95 H. Singh, M. Marley-Hines, S. Chakravarty and M. Nath, *J. Mater. Chem. A*, 2022, **10**, 6772–6784.

96 H. Shin, S. Geum, J. Lee, M. Shin, K. M. Ok, S. J. Kwon and J. Do, *Bull. Korean Chem. Soc.*, 2024, **45**, 920–928.

97 Y. Shin and S. Park, *Bull. Korean Chem. Soc.*, 2024, **45**, 23–31.

98 X. Yang, W. Sun, B. Li, Y. Dong, X. Huang, C. Hu, M. Chen, Y. Li and Y. Ding, *J. Colloid Interface Sci.*, 2024, **655**, 779–788.

99 X. Chai, X. Du and X. Zhang, *Fuel*, 2024, **377**, 132781.

100 A. BaQais, M. Shariq, M. A. Qamar, D. Alhasmialameer, A. F. Alharbi, H. A. Althikrallah, M. R. Alrahili and K. S. Alrashdi, *Diam. Relat. Mater.*, 2024, **147**, 111343.

101 M. Shakeel, M. Arif, G. Yasin, B. Li and H. D. Khan, *Appl. Catal., B*, 2019, **242**, 485–498.

102 B. Zhang, J. Li, Q. Song and H. Liu, *Int. J. Energy Res.*, 2022, **46**, 12406–12416.

103 G. Zhang, J. Xing, Y. Zhao and F. Yang, *J. Colloid Interface Sci.*, 2021, **590**, 476–486.

104 O. Ambriz-Peláez, J. Béjar, A. D. Delgado, C. Rodríguez-González, C. M. Ramos-Castillo, L. Álvarez-Contreras, M. Guerra-Balcázar and N. Arjona, *FlatChem*, 2024, **45**, 100664.

105 W. Ma, Y. Zhang, B. Wang, J. Wang, Y. Dai, L. Hu, X. Lv and J. Dang, *Chem. Eng. J.*, 2024, **494**, 153212.

106 G. Ma, J. Ye, M. Qin, T. Sun, W. Tan, Z. Fan, L. Huang and X. Xin, *Nano Energy*, 2023, **115**, 108679.

107 J. Chen, X. Li, Y. Li, Y. Li, B. Hu, X. Liu, Q. Qi, R. Wang, Y. Yang and Y. Liu, *J. Environ. Chem. Eng.*, 2024, **12**(5), 113635.

108 F. Yang, G. Dong, L. Meng, L. Liu, X. Liu, Z. Zhang, M. Zhao and W. Zhang, *Int. J. Hydrogen Energy*, 2024, **77**, 589–597.

109 L. Zhu, R. Wang, X. Liu, S. Yang, H. Liu, B. Xing and K. Wang, *Appl. Surf. Sci.*, 2024, **656**, 159711.

110 Y. Wang, Q. Dong, X. Du and X. Zhang, *Int. J. Hydrogen Energy*, 2024, **69**, 895–904.

111 Y. Luo, P. Wang, G. Zhang, S. Wu, Z. Chen, H. Ranganathan, S. Sun and Z. Shi, *Chem. Eng. J.*, 2023, **454**, 140061.

112 G. E. Ayom, M. D. Khan, F. M. de Souza, W. Lin, R. K. Gupta and N. Revaprasadu, *J. Energy Storage*, 2024, **97**, 112882.

113 S. V. Terlapu and R. Bauri, *Sustainable Energy Fuels*, 2024, **8**, 5195.

114 Z. Shui, H. Tian, H. Mu, L. Xu, X. Gao and X. Chen, *Inorg. Chem. Front.*, 2025, **12**, 2783.

115 A. Hanan, D. Shu, U. Aftab, D. Cao, A. J. Laghari, M. Y. Solangi, M. I. Abro, A. Nafady, B. Vigolo, A. Tahira and Z. H. Ibupoto, *Int. J. Hydrogen Energy*, 2022, **47**, 33919–33937.

116 A. Hanan, M. N. Lakhan, D. Shu, A. Hussain, M. Ahmed, I. A. Soomro, V. Kumar and D. Cao, *Int. J. Hydrogen Energy*, 2023, **48**, 19494–19508.

117 S. Noor, F. Ahmad, M. I. Khan, A. Shanableh, S. Khan, S. Manzoor, S. M. Osman and R. Luque, *Appl. Organomet. Chem.*, 2024, **38**, 7676.

118 A. Hanan, M. N. Lakhan, R. Walvekar, M. Ubaidullah, A. A. Al-Kahtani and M. Khalid, *Int. J. Hydrogen Energy*, 2025, **104**, 407–415.

119 H. Xue, J. Wang, Z. Zhang, X. Li, J. Sun, Y. Zhang, Y. Bai and Z. Li, *Appl. Surf. Sci.*, 2024, **648**, 159058.

120 L. Mu, J. Ying, Y. Ou, Z. Wang, Y. Liu, N. Zhao, M. Xue, Y. Dai and G. Zhao, *J. Colloid Interface Sci.*, 2025, **688**, 106–117.

121 A. M. Shah, K. H. Modi, P. M. Pataniya, K. S. Joseph, S. Dabhi, G. R. Bhadu and C. Sumesh, *ACS Appl. Mater. Interfaces*, 2024, **16**, 11440–11452.

122 S. Mao, L. Ye, S. Jin, C. Zhou, J. Pang and W. Xu, *Inorg. Chem.*, 2024, **63**, 6005–6015.

123 Z. M. Almarhoon, K. Jabbour, S. Manzoor, S. I. A. Shah, M. F. Ashiq, M. Y. Ur Rehman, M. F. Ehsan, M. Najam-ul-Haq and M. N. Ashiq, *Fuel*, 2024, **363**, 130919.

124 N. Rasool, H. A. Alyousef, A. W. Alrowaily, B. M. Alotaibi, A. G. Al-Sehemi and K. Ahmad, *J. Korean Ceram. Soc.*, 2025, **62**, 46–55.

125 S. Long, X. Peng, L. Han, Q. Luo, S. Xiao, J. Feng, Y. Sui, X. Zeng, Y. Zhang and P. Dong, *Appl. Surf. Sci.*, 2025, **690**, 162600.

126 X. Fu, L. Zhang, X. Zhu, S. Zhu, Y. Min, Q. Xu and Q. Li, *Appl. Surf. Sci.*, 2023, **613**, 156087.

127 Y. Guo, M. Chen, Y. Wang, X. Lu, J. Wu and X. Tang, *ACS Appl. Nano Mater.*, 2024, **7**, 8351–8361.

128 Y. Luo, Q. Wang, Y. Chen, J. Feng, L. Wang, Y. Jiang, L. Li, X. Xu and J. Feng, *ACS Sustainable Chem. Eng.*, 2023, **11**, 8075–8083.

129 A. Plavniece, K. Kaare, D. Simkunaitė, A. Balciunaite, V. Jasulaitiene, G. Niaura, A. Volperts, G. Dobele, L. C. Colmenares-Rausseo, I. Kruusenberg, L. Tamasauskaite-Tamasiunaite and E. Norkus, *Catalysts*, 2024, **14**, 92.

130 A. Mariappan, R. K. Dharman, T. H. Oh, S. Prabu and K. Y. Chiang, *Mater. Chem. Phys.*, 2023, **309**, 128321.

131 U. Aftab, M. Y. Solangi, A. Tahira, A. Hanan, M. I. Abro, A. Karsy, E. Dawi, M. A. Bhatti, R. H. Alshammari, A. Nafady, A. Gradone, R. Mazzaro, V. Morandi, A. Infantes-Molina and Z. H. Ibupoto, *RSC Adv.*, 2023, **13**, 32413–32423.

132 F. N. I. Sari, Y. C. Lai, Y. J. Huang, X. Y. Wei, H. Pourzolfaghar, Y. H. Chang, M. Ghufron, Y. Y. Li, Y. H. Su, O. Clemens and J. M. Ting, *Adv. Funct. Mater.*, 2024, **34**, 2310181.

133 L. Diao, C. Zhang, X. Yang, N. Zhang, J. Ren, D. Li and D. Yang, *Mater Today Sustain.*, 2023, **23**, 100408.

This journal is © the Owner Societies 2025

Phys. Chem. Chem. Phys., 2025, **27**, 17099–17115 | **17115**